Title
Simulation of Glass: from Production to Long-term Utilization

Author
Wang, Zhe

Publication Date
2022

Peer reviewed|Thesis/dissertation

UNIVERSITY OF CALIFORNIA

Los Angeles

Simulation of Glass: from Production to Long-term Utilization

A dissertation submitted in partial satisfaction of the requirements for the degree

Doctor of Philosophy in Civil Engineering

by

Zhe Wang

2022

ABSTRACT OF THE DISSERTATION

Simulation of Glass: from Production to Long-term Utilization

by

Zhe Wang

Doctor of Philosophy in Civil Engineering

University of California, Los Angeles, 2022

Professor Mathieu Bauchy, Chair

Glass is one of the most important and frequently used materials due to its special properties: its hardness and transparency makes it an ideal material for windows, and its stability makes it a great candidate for immobilizing radioactive nuclear waste, etc. As a result, almost all aspects of glass ranging from its fabrication, properties and application, characterization, to stability and destruction have been hot topics of material science research for a long time. Among all researching methods, molecular dynamics (MD) simulation is a new emerging technique that has been applied more and more to glass research in modern years thanks to its advantages over conventional experimental methods such as high efficiency, high accuracy and low cost.

This thesis focuses on using MD simulations to evaluate glass properties from two main aspects: 1) the equivalence of glasses produced from modern methods such as vapor deposition, sol-gel condensation and irradiation and those fabricated from conventional melt-quenching, and 2) the effects of temperature, pH and glass composition on zeolite precipitation during the nuclear waste immobilization glass dissolution process. The thesis is thus divided based on these two topics.

In Chapter I, we aim to compare the equivalence of SiO_2 glasses obtained from MD-simulated vapor deposition, sol-gel condensation and irradiation processes and the melt-quenched glasses. That is, to evaluate whether these glasses can (available) or cannot (forbidden) be obtained by using the traditional melt-quenching method by changing the cooling rate. We will show that the availability of glasses can be determined and explained by observing the medium-range structural features and the energy landscape of the atoms.

In Chapter II, we explore another important field of glass application: the nuclear waste-immobilization glass dissolution. Though vitrification: the process of melting and mixing radioactive nuclear waste and glassy materials, is widely considered the best way of treating nuclear waste due to the extraordinary stability of glasses, observation of continuous glass dissolution (alteration resumption process, or stage III of the nuclear waste-immobilization glasses dissolution process) is reported in many experimental cases which will lead to nuclear waste leakage. Though the exact reason of alteration resumption is still being discussed, it is generally believed that this phenomenon is closely related to the precipitation of secondary phases like zeolites. Based on *ab initio* MD simulations, we first construct a complete methodology to calculate the thermodynamic properties (enthalpy and entropy of formation, heat capacity, etc.) of any zeolites given its composition and lattice structure. Moreover, with these

thermodynamic data of zeolites, we use Gibbs free Energy Minimization (GEM) simulation to build a database of zeolite precipitation under various temperatures, pHs and initial glass compositions. Finally, we manage to train a machine learning (ML) model using the precipitation database that can predict zeolite formation given the aforementioned conditions as inputs.

The dissertation of Zhe Wang is approved.

Gaurav Sant

Jaime Marian

Sanjay K. Mohanty

Mathieu Bauchy, Committee Chair

University of California, Los Angeles

2022

Table of Contents

List of Tables

List of Figures

Acknowledgment

The past 6 years were like a dream.

On my last day in Northwestern, Prof. Mark Hersam said to me: Going for a PhD is only for the bravest of human beings: you are not just trying to get a diploma, the future and the great burden of pushing forward our understanding of the universe now fall on your shoulders.

“朝闻道，夕死可也。”

“Life is worth everything when you find the way.”

I cannot say the things I have done in these 6 years made a difference to our race or the universe, but they did change me by a lot. More important than the research I did and the papers I wrote, those countless moment of struggling about being fast or being true, the endless time of not knowing where tomorrow leads to, when I somehow survive, I find that they taught me what is life. I feel extremely blessed to have devoted the best years of my life into this incredible journey, and would give my upmost gratitude to my PhD career: thank you for teaching me the way to do things, the way to be a MAN.

“世不稀管仲之才，而稀鲍叔牙之识人也。”

“More valuable than gold, is the one who can find it.”

I must thank my advisor: Prof. Mathieu Bauchy for offering me this opportunity during my darkest hours. It was hard to describe how hard it was to continue my PhD studying when I had

to look for a new research group almost a year and a half after I started. It was impossible to restart with all the courses, setting up new research plans that I have never learned from, and successfully finishing the preliminary and oral exams without the help and advice from Prof. Bauchy. It was also an honor that I could join Prof. Bauchy in the GOMD, the conference for young glass researchers in Penn State, and many more academic seminars to see, to learn, and meet with the vanguards in glass science and industry. Though the most common case it may be, listening to Prof. Bauchy's observation on every detail in a plot, his suggestions on what a reasonable next step would be, his logical and accurate thinking during a group meeting has changed and formed my way of considering and doing things. It's my fortune to meet him as not just an advisor to my work, but also my values, my life.

I would like to also thank Prof. Sant, Prof. Marian, and Prof. Mohanty for your suggestions on my research topics and methods, especially during this hard time of the global pandemic.

"子曰：三年无改于父之道，可谓孝矣。"

"The real filial piety is to have the father's bearings after his death."

I owe my greatest gratitude to my parents, whose financial support and meticulous caring is the base of my adventure. To live my own life and chasing dreams alone in a place half the Earth away from home is never easy, but whenever I am about to lose faith, I know that there is a land flowing with milk and honey. The old Chinese saying goes: there is no war without provisions. At this moment when I could finally say I am financially independent, I want to proudly tell my dear father and mother: I am not just an adult, I am a man now!

“君子之交淡如水，小人之交甘若醴。”

“A spiritual friend is a real friend.”

I feel lucky to know so many friendly people who are willing to share their research thinking, industrial experience, their dreams, their goals and their taos with me. I feel even luckier that these are not because of anything worldly. “Big minds talk about ideas. Ordinary minds talk about business. Small minds talk about people.” I would take this chance thank all of those who I discussed ideas with.

I thank my colleagues from PARIS lab. Qi, Zhou, Kai, Yuhai, Ruoxia, Longwen, Tao, Yu, Zhangji, Han, Cheng, Yao, Pragathi, Xin and Biyun, thank you for spending these years beside me in and out of the office. It’s such a pleasure to have shared thoughts with you on research, coding, career, and so many more things in life. I hope we can stay connected ever in the future.

I thank my mate Peiqi for always happily discussing any interesting or rather, strange things in this world. See you again in San Jose.

I thank my mate Ruxi for teaching me how to be a TA and a group player, how to study and do research, how you design what to do about your career, and our time feeling awkward about recent films.

I thank my big brother Yichao for teaching me how be a researcher, how to be a grown man with responsibility, and the way to be kind to all people and things around me. Those who never give up being a researcher are the people I will always admire. I hope you all the best in pursuing an adventurous academic career and a happy life with my big sister Ruikun.

I thank my mate Chen for our discussion on simulations, physics, math, basketball, and Anime. The experience of hunting for jobs and encouraging each other would always be my

irreplaceable memory. Even when the Chinese basketball and football teams only have two fans in the world, it will be us.

I thank my friend Shiqi Dong for encouraging me and making it possible for me to continue with my PhD career. It's hard to imagine what these past few years would have been without your help. I can't wait to join you again in San Jose!

I thank my mate Shiqi Zheng, Haotian, Ray, and Jin for teaching me how to do research and live in a foreign country. Your suggestions on my academic and post-academic career, our time trying out restaurants and watching Marvel films are the treasure of life for me.

I thank Chuancheng, Jian, Hao, Yuan, Guangyan, Yun-Chiao for your help and suggestions on fabricating devices and choosing the best career. Though my PhD turns out to be about something else, now I am proudly back to the fields I would happily devote my life to!

I thank Le, Zhengxu, Haowen, Guangwei, Peter for teaching me about the knowledge, the way, and the attitude to be a device researcher. The hard time we have been together taught me how to stay strong in the darkest hours of life.

I thank Prof. Krishnan, Prof. Smedskjaer, Prof. Mauro, Prof. Jincheng, Prof. Gin, Prof. Ryan, Prof. Bu Wang, Prof. Jian Huang, Peng for your guides on glass research, how to be a forerunner in the field of simulation, material science and chemistry.

I thank my cousins Haohao, Shang, Yuan and Pengpeng for encouraging me and sharing any of my stories with me when I need you the most.

I thank my friends in China: Auntie Yuntian, Auntie Fan and Uncle Meng, Sihan, Han, Ruitao, Jianxue, my friends in the East: Daheng, Yixing, Qishen, Xinhao, Songge. Thank you for all your help in the past few years, I appreciate and still miss the time we were together and hope that we can meet again in the future somedays.

“独上北皋远望，残月映星光。旦惜知己如暮芳，昨日落，今日香。”

“I, now must leave, with tears in my eyes and heart in peace, not knowing what to speak.”

VITA

EDUCATION

Northwestern University, Evanston, IL, USA Sep. 2015 – June. 2016

M.S.: Material Science and Engineering GPA: 3.76/4.00

Beijing University of Aeronautics and Astronautics (BUAA), Beijing, China Sep. 2011 – June. 2015

B.S.: Applied Physics GPA: 3.75/4.00 (Major: 3.80/4.00)

RESEARCH EXPERIENCE

UCLA Los Angeles, CA

Graduate Research Assistant (Advisor: Prof. **Mathieu Bauchy**) Feb. 2018 – Sep.2022

Zeolite Formation Prediction based on Machine Learning Models:

- By utilizing Python and Matlab ML packages, build models that can predict zeolite precipitation under various conditions (pH, temperature, etc) using data from Gibbs energy minimization simulations.
- These results can be used to explain nuclear-waste immobilization glasses dissolution (paper in preparation).

Investigation of the Nature of Vapor Deposited Glasses:

- Simulate the physical vapor deposition formation of glassy silica based on Reactive molecular dynamics and compare them with conventional melt-quenched glasses to show that its nature depends on the substrate temperature.

Graduate Research Assistant (Advisor: Prof. **Yang Yang**) Jul. 2017 – Dec.2017

Solution-processed InGaZnO (IGZO) thin-film transistor:

- Fabricate solution-processed IGZO and Indium oxide Thin-film transistors (TFT) in cleanroom.
- Boost stability and performance of sol-gel IGZO TFT by varying chemical composition.
- Design series of code for current-voltage data analysis and photo mask of TFT array and OLED patterns.

Graduate Research Assistant (Advisor: Prof. **Xiangfeng Duan**) Sep. 2016 – Jun.2017

2-D material and devices:

- Fabricate GeAs/MoS_2 heterostructure diodes and single-molecule FETs.

INTERNSHIP EXPERIENCE

Amap.com Beijing, China (Remote)

Deep Learning Internship Feb. 2022 – May. 2022

Design to Code (d2c) Model Construction:

- Written in Python and by using the Keras packages, realize a group of neural network (based on models like VGG16, and layers like LSTM, GRU, etc.) models that have functions ranging from predicting sentences from text images to realizing fonts and simple shapes like buttons and horizontal lines, then converting them into HTML texts.
- Training and testing images are borrowed from Google image and Figma.com.
- Preliminary models reach over 70% accuracy overall evaluated based on BLEU scores while being tested on a test set of about 300 designs with their original HTML codes**.**

PUBLICATIONS

Synthesis, Structure, Multiband Optical, and Electrical Conductive Properties of a 3D Open Cubic Framework Based on $[Cu_8Sn_6S_{24}]^{z-}$ Clusters
X Zhang, Q Wang, Z Ma, J He, Z Wang, C Zheng, J Lin, F Huang
Inorganic Chemistry 54 (11), 5301-5308

Atomistic origin of the passivation effect in hydrated silicate glasses
T Du, H Li, Q Zhou, Z Wang, G Sant, JV Ryan, M Bauchy
npj Materials Degradation 3 (1), 1-7

Synthesis, structure, magnetic and photoelectric properties of Ln 3 M 0.5 M′ Se 7 (Ln= La, Ce, Sm; M= Fe, Mn; M′= Si, Ge) and La 3 MnGaSe 7
J He, Z Wang, X Zhang, Y Cheng, Y Gong, X Lai, C Zheng, J Lin, F Huang
RSC Advances 5 (65), 52629-52635

On the equivalence of vapor-deposited and melt-quenched glasses
Z Wang, T Du, NM Anoop Krishnan, MM Smedskjaer, M Bauchy
The Journal of Chemical Physics 152 (16), 164504

Topological origin of phase separation in hydrated gels
C Zhao, W Zhou, Q Zhou, Z Wang, G Sant, L Guo, M Bauchy
Journal of Colloid and Interface Science 590, 199-209

Challenges and opportunities in atomistic simulations of glasses: a review
H Liu, Z Zhao, Q Zhou, R Chen, K Yang, Z Wang, L Tang, M Bauchy
Comptes Rendus. Géoscience 354 (S1), 1-43

1 Introduction

1.1 Background

1.1.1 Glass

Glass is one of the most widely used as well as the most deeply explored materials in the world [1–11]. This is mainly because of its unique and useful properties that, combining together with each other, makes glass an irreplaceable building block for many aspects of the modern society [1,3,7,12,13]. These properties include:

1) Transparency: the property that let photons pass through without reflection nor absorption due to the high energy gap of glass atoms. This makes glass the top choice in any situation where light transmission is required while other substances will be blocked off, like windows and containers.
2) Hardness [1,8]: the property that stop glass from deformation. It is important since in many cases we want glass devices to keep its original shape: we don't want a bending building or a tea kettle that leans and pours tea by itself.

3) Stability [12,14,15]: the property that makes glass highly resistible to extreme extrinsic effects. Chemically, many glasses, like the most frequently used aluminosilicate glasses, are stable in a wide range of pH and do not react with most substances we meet in daily life. Physically, thanks to its highly disordered inter-atomic structure, glass can absorb high level irradiation which makes it very useful in fields like nuclear waste treatment. In fact, vitrification is currently the most widely used nuclear waste solution around the world.
4) Low cost: many glasses at room temperature, such as SiO_2 and B_2O_3, are cheap materials that has ample nature storage (90% of the Earth's crust is silicate). And the fabrication process of glasses, through many years of upgrading and refinement, has come to a stage that is fast, energy-sufficient, environmental-friendly and costs low.

The interesting properties of glass make it one of the hottest research topics of material science through history and until today. New findings in glass science usually bring great benefit for both scientific research and industrial applications.

1.1.2 Molecular dynamics simulation of Glasses

Molecular dynamics (MD) simulation is a promising new researching method that emerges along with the development of modern computational power [16–24]. It is a group of computer algorithms that is based on either classical or quantum dynamical mechanics where a system of atoms are first generated, and their trajectories of movements are then calculated from equations of motion.

At the same time, a MD process must also have suitable initial and boundary conditions, proper interatomic potentials, and satisfy thermodynamical constraints. Different from other simulation algorithms (e.g. Monte Carlo), MD is:

1) Deterministic: if the state of a system is known at a given time, its future can be predicted.
2) Mechanistic: MD explores the configurational space of a system by simulating its real dynamics rather than through fictitious trial moves. As a result, MD has the power to assess the dynamical properties of matter.

With molecular dynamics, it is possible to investigate material behaviors at microscopic scales with high efficiency and accuracy. Compared to traditional experimental methods, it has the advantage of low cost, fast completion, concurrency and the fact that the simulation can be stopped and continued from any point along the way.

Though a useful method as it is, while coming to the specific case of glasses, the major difficulty for MD simulations falls into glasses' disordered structure [17,23,25,26]. Essentially, glass has short-range order, partial medium-range order and complete long-range disorder. This means that, in order to realistically simulate glasses, one must not include periodic boundary conditions which will, at a certain level, make the atomic system ordered. However, till today, computational power is not strong enough to simulate a complete disordered system at a macroscopic level (typical computational power limit: classical ~ 10k atoms, *ab initio* ~100 atoms) [27,28], researcher thus must make reasonable approximation and appropriate simplification to all the required data and algorithms in MD for simulations of glasses [27–29]. Although MD cannot reach complete

accuracy for glass simulations, many meaningful results have been obtained from MD research over the years that successfully benefit the production and application of glasses in industry.

1.1.3 Nuclear waste immobilization glass dissolution

As mentioned earlier, for reasons of price, efficiency, and ease of use, one of the most general and widely used method to treat radioactive nuclear waste is vitrification [30–34]: the process where the liquid waste is mixed with boro(alumino)silicate melt and the mixture is then cooled to become a glassy compound. This is because, unlike crystals or other ordered materials, the disordered structure of glass networks has the ability to absorb high irradiation energy from the internal nuclear waste and still stay at glassy form without being damaged [4,11,31,35–37]. Meanwhile, externally, glasses are particularly stable against chemical erosion that may cause its radioactive content to leak out. Finally, the vitrified product undergoes deep geological disposal and it is expected that the nuclear glass would be durable enough to withstand underground environmental corrosion, where water is considered to be the main cause, for millions of years [4,8,31,33,36].

The dissolution process of nuclear glass in groundwater (depicted as the fraction of glass that is altered by corrosion and the rate of this process) can be illustrated in Figure 1.1-1 [38], where it is typically described to have 3 stages that are controlled by different limiting mechanisms:

Stage I: In unsaturated conditions, glass dissolution can occur through hydration due to water diffusion through the glass, exchanges between mobile ions within the glass and H^+ species (interdiffusion), and hydrolysis of the covalent bonds forming the boro(alumino)silicate network. Stage II: This results in an initially high dissolution rate (forward rate). At higher reaction progress, parts of the hydrolyzed species re-condense to form a low-porosity amorphous hydrated layer called a "gel layer," which can be passivating and transport-limiting for aqueous species. The formation of this layer and the diminishing affinity of the hydrolysis reaction result in a decrease in the dissolution rate (rate drop regime). This is where we hope the story ends since the alteration rate comes down to a very low level and the nuclear glass can stay stable for a long duration of time.

Stage III: Under certain conditions, it is observed that the main components of the passivation layer (mostly Al and Si) can be consumed by the precipitation of secondary crystalline phases. Depending on the type of secondary phases that form, two distinct regimes can be observed: (i) a "residual rate regime", when a quasi-steady state is reached between the formation the crystalline phases (usually clay-type) and the destabilization of the passivation layer, or (ii) an "alteration resumption regime," in the case of the massive precipitation of secondary phases (usually zeolites or C–S–H), which destabilizes the passivation layer. The latter case, the destabilization of the passivation gel trend to reinitiate the dissolution of the glass—the dissolution rate increasing by a factor 20-to-2000 with respect to the residual rate. This will inevitably lead to the accelerating deterioration of nuclear glass and potential leakage of radioactive waste.

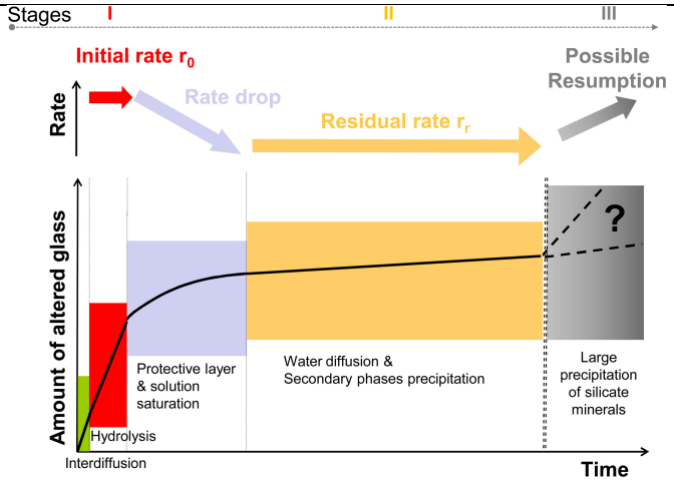

Figure 1.1-1

Glass corrosion stages and related rate limiting mechanisms: initial dissolution rate, rate drop, residual rate, and alteration resumption. (plot from Stéphane Gin [4])

1.2 Motivation and outline

This thesis will mainly be unfolded around two topics that are related to the production (birth) and long-term utilization (failure mechanisms, or death) of glass separately and thus divided into two chapters:

Chapter I. The equivalence of glasses produced from modern methods and melt-quenched glasses.

Modern technology has brought about many exciting new methods of glass fabrication.

Modern technology has introduced many new methods of glass fabrication that often have various advantages over the conventional melt-quenching (MQ). In this thesis, we simulate the following methods using classical mechanics:

a. Vapor deposition (VD): a method where particles undergo transitions from a condensed phase to a vapor phase and then back to a thin film condensed phase. Depending on the way the particles are adsorbed onto the substrate, there are physical (where particles are attached to the substrate through Van der Waals potential) and chemical (where vapor atoms or molecules are grasped by substrate materials through chemical reactions) vapor depositions. VD has been widely applied to the fabrication of all kinds of thin-film materials such as glass, alloy, and polymer, etc. In this thesis, we simulate a physical vapor deposition process of SiO_2 using a melt-quenched silica glass as its substrate.
b. Sol-gel condensation (SG): a method based on the continuous "drying" of hydrated gels (shown in Figure 1.2-1). The sol-gel condensation process is usually carried out in these steps: First, a solution that contains the precursor of the desired material is prepared. Next, the system is heated to and maintained at an elevated temperature for the condensation reaction to happen. Water in the solution is evaporated at the same time. Finally, the system is cooled and relaxed to form glass. The heating and cooling processes are usually done multiple times to ensure complete removal of water. Due to its advantage of requiring much lower cost and temperature compared to traditional methods like melt-quenching, SG is frequently used to synthesize homogeneous glasses. Here, we simulate a SG condensation process that forms a SiO_2 glass network.

c. Irradiation: a technique based on the idea of producing disordered materials by introducing defects into crystalline lattices. One of the most straightforward ways to generate defects is irradiating particle rays onto the crystal atoms. In this thesis, we simulate a neutron irradiation of process on quartz that generally transforms into SiO_2 glass when high dose of radioactive energy is absorbed.

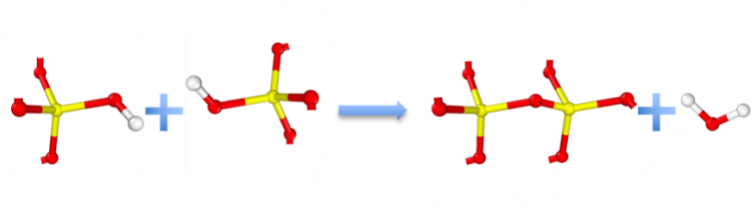

Figure 1.2-1

Sol-gel condensation mechanisms: two $Si(OH)_4$ precursors connect to each other by creating one bridging oxygen (BO) and a water molecule [39].

At last, to make a fair and convincing comparison, we also simulate a group of melt-quenched silica glasses with different cooling rates.

Though earlier works has practiced the simulation of these methods and discussed the properties of resulting glasses, one important question hasn't yet to be answered to our knowledge: can these glasses be obtained from using melt-quenching by only tuning the cooling rate (available)? Or are they something else that are completely different from melt-quenched glasses

(forbidden)? Answering this question will not only explain the nature of glasses produced by these new methods, but also give us a hint on how their characteristics can affect the resulting products and, in turn, the optimal way and situation to use them.

To simplify the problem for this research, we will use SiO_2 for all discussions. For each method, we will start by describing every simulation detail and their purposes. We then use various algorithms to analyze the microscopic properties of the resulting glasses: average atomic potential energy, Voronoi volume, ring-size distribution, interatomic energy barrier, etc. Based on the mapping of these features, we are able to determine whether a glass falls into an available or a forbidden area and interpret this availability.

Chapter II. The effects of temperature, pH and glass composition on zeolite precipitation during the nuclear waste immobilization glass dissolution process. The thesis is thus divided based on these two topics.

As pointed out before, the alteration resumption process of nuclear waste immobilization glass has been demonstrated to be closely related to the precipitation of secondary phases including zeolites. Thus, knowing the conditions of zeolite formation is crucial to understand the long-term stability of nuclear glass and potentially prevent its dissolution in ground water. To do this, our work in this thesis can be divided into three major steps:

1. Developing a methodology that can accurately calculate the thermodynamic properties (enthalpy, entropy of formation, heat capacity and Gibbs free energy) of all zeolites through high-through put MD simulations.
2. Using the data from step 1, unambiguously identifying the propensity for various zeolite precipitation as a function of solution conditions (glass composition, pH and temperature) by applying the Gibbs Energy Minimization (GEM) simulations.
3. Collecting the data from step 2 and train a machine learning (ML) model that has the capability to predict zeolite precipitation based on the input of aforementioned solution conditions.

For step 1, we use *ab initio* molecular dynamics (AIMD) for all calculations. This is because, first, AIMD is much more accurate than classical MD, which is necessary for the validation using experimental data in this research; second, zeolites are crystals whose lattice structures can be determined, and periodic boundary conditions can thus be applied, which ideally only requires one lattice cell and solves the problem of high computational cost of First Principle simulations. We meet a few interesting unforeseen hard points while constructing this methodology such as the partial atomic site occupancy of some zeolite species, and the treatment of zeolitic water molecule. However, these problems turn out to be heuristic because, upon solving them, it opens up the way of approaching many similar difficulties from simulating other classes of materials mentioned in the literature.

In step 2, we use a software called Gibbs Energy Minimization Selektor (GEMS) which, given the necessary input of reactants, environmental parameters like pH and temperature, and the pool

of all interested products with their thermodynamic data, can calculate the amount of precipitation by simulating the process of reaching chemical equilibrium (by minimizing the total Gibbs free energy). We mainly care about the starting pH of zeolite precipitation for various glass compositions and temperatures, which is the pH where we start to get nonzero product data for all every zeolite.

At last, step 3 is a machine learning problem where we use the composition and temperature data from step 2 as input and starting pH of precipitation as output. We change the data for training and testing every time and continuously tune the hyperparameters of the model for the lowest prediction error. At the same time, by evaluating the SHAP data of the model, we can also approach how the input factors can influence the starting pH and validate it with existing papers. By going through these steps, we not only gain a better understanding of the mechanisms of stage III of nuclear glass dissolution, but also show that the complete methodology we develop can also be helpful to calculate, simulate and predict the formation of many other aluminosilicate materials beside zeolites. Moreover, we use the abundant data from our simulations to build a database of zeolite thermodynamic and solution kinetic parameters. This will greatly enrich the experimental data of low-temperature zeolite synthesis that is usually scarce due to the great difficulty of synthesizing zeolites under room temperature. By summarizing and analyzing the data, we will also show some interesting observations that can help explain the behavior of zeolitic water molecule and its contribution to volume-based thermodynamics.

1.3 Contributions

To sum up, the contribution of this thesis is as follows:

- We were among the first who tried to connect different glass fabrication techniques with melt-quenching. There are many former works about the simulation of these glass synthesis methods, but few has compared them with the most commonly used MQ process, which has great meaning in determining their industrial value.
- We constructed a complete methodology in simulating the thermodynamic properties of zeolites. This not just opened up a path towards high-throughput data harvesting that can greatly make up to the scarce experimental data of low temperature zeolite synthesis but can also be extended to other similar crystalline materials, especially those with partial atomic site occupancy and crystalline water.
- We pioneered in building a systematic database of zeolite which can be used to determine the nucleation and growth kinetics of zeolite crystallization as a function of solution composition, pH and temperature, and potentially benefit any research around zeolite chemical behaviors in the future.

2 Chapter I Equivalence of glasses produced by modern methods and melt-quenched glasses

2.1 Overview of this chapter

This chapter will focus on comparing the SiO_2 glasses obtained from vapor-deposition, sol-gel condensation, and irradiation processes with those made by the melt-quenching method and the discussion of their availability and the structural reasons behind it.

We will first give a thorough introduction of the background, the MD simulation details, the force field we use and the analyzing methods (RINGS, ART software, etc). Next, we will discuss the results based on the mapping of various structural and stability features (potential energy, Voronoi volume, ring eccentricity, ring-size distribution, ring floppy modes and so on) of each glass. We will conclude this chapter with in-depth analysis on the nature of these methods and give some suggestions on future simulations.

2.2 Introduction

With the development of modern technologies, glasses can be fabricated through various new fabrication methods beside the traditional melt-quenching. Many of these glasses possess interesting characteristics and may potentially be more stable and durable than conventional glasses.

We will focus on three methods in this chapter: 1) vapor deposition 2) sol-gel condensation 3) irradiation. We choose these methods not just because they are shown to have unique properties,

but also for the fact that they appear in many earlier works both experimentally and by simulation where there are sufficient data for validation and comparison.

2.2.1 Vapor deposition

If quenched fast enough, liquids can avoid crystallization and remain in the metastable supercooled liquid state [5]. At the glass transition, the relaxation time eventually exceeds the observation time—so that melts experience a kinetic arrest and enter the out-of-equilibrium glassy state [1,2]. As out-of-equilibrium phases, the structure and properties of glasses depend on their history. In particular, the use of lower cooling rates results in the formation of more stable glasses that occupy lower states in the energy landscape [5]. As an alternative route to melt-quenching, vapor deposition can yield ultrastable glasses [12,40]—the degree of stability depending on the substrate temperature and deposition rate [15,40–43]. The ultrastable nature of vapor-deposited glasses has been suggested to result from the enhanced mobility of the atoms at the surface of the deposited glass as compared to those in the bulk, thereby allowing deposited glasses to access lower energy states in an accelerated fashion [13,44]. However, it remains unclear whether ultrastable vapor-deposited glasses are allowable (i.e., equivalent to glasses formed with a very slow cooling rate) or forbidden (i.e., glasses that cannot be formed via any thermal route) [6], which is going to be the main focus of this chapter as well as for the other two methods.
Here, based on reactive MD simulations, we simulate and compare a series of (i) vapor-deposited SiO_2 glasses associated with varying substrate temperatures and (ii) melt- quenched SiO_2

freestanding films—so that all these systems exhibit a free surface and, hence, only differ from each other by their method of synthesis (i.e., vapor deposition vs. melt-quenching). The fact of considering melt-quenched freestanding films rather than bulk glasses allows us to filter out the effect of the surface in our comparison between vapor-deposited and melt-quenched glasses [44,45]. Importantly, we demonstrate that vapor-deposited glasses are allowable in the case of high substrate temperatures but forbidden for low substrate temperatures. We find that the forbidden nature of glasses deposited on low-temperature substrates is primarily encoded in their ring size distribution.

2.2.2 Sol-gel condensation

The sol–gel method has been widely applied to the synthesis of silicate materials, including bio-glasses, zeolites, and various mesoporous clay phases [3,7,8,46,47]. Basically, it is a two-step process: 1) colloidal precursors are dispersed in a liquid solution and gradually aggregate to form a three-dimensional network through condensation reactions [8]; 2) under elevated temperatures, a solid gel can be obtained after subsequent dehydration treatment. Unlike the melt-quenching method, sol–gel condensation does not involve the melting of crystalline materials and thus only requires lower synthesis temperature and lower costs. It has also been shown that the sol–gel route can be used to synthesize unusual glasses that are challenging to prepare using the melt-quenching method due to their propensity for crystallization of phase separation [9,48].

Though a lot of efforts have been paid to understand the mechanism of the polymerization of orthosilicic acid $Si(OH)_4$ monomers in aqueous solution [49–54] and the atomic structure of silica gels at each stage, the stability and the available or forbidden nature of sol-gel glasses have never been systematically investigated. This is due to the experimental difficulties in characterizing the structure of disordered media (especially so when the structure is evolving over time). Similar challenges are present for simulation methods where *ab initio* molecular dynamics (AIMD) is limited by small system sizes and time scales, and classical MD lack the ability to accurately describe the activity of silicate materials in aqueous environments.

As a hopeful alternative, the reactive force-fields (e.g., ReaxFF) have been proved to have the capability of modeling large atomic systems while having much higher computational efficiency than AIMD [19,55,56]. In fact, the ReaxFF potential has already been used to explore sol-gel condensation mechanisms and successfully capture the kinetics of silicate glasses. Here, using ReaxFF, we first repeat the method used by Du *et al.* to simulate the synthesis of a low-temperature relaxed sol-gel glass [39], then compare its stability, microscopic structural properties, and availability with the other glasses (vapor deposition, melt-quenching, irradiation). We show that the sol-gel glass obtained here can be even more stable than slowly quenched glasses. We also demonstrate that the sol-gel condensation process leads to a large number of elliptical silica rings compared to melt-quenching that have more floppy modes thus higher flexibility topologically, which may also be used to explain its ultra stability.

2.2.3 Irradiation

As mentioned in the earlier part of this thesis, glasses are one of the most popular materials to immobilize nuclear waste due to its stability, durability, and low cost. That being mentioned, glasses are not perfect and continuous irradiation may still cause damage in the long term. As a result, understanding irradiation-induced damage is of great importance for glass applications in relevant fields: nuclear plant safety, nuclear fuel form clarification and containment, as well as the controlled doping of semiconductors that is used in nuclear fusion plants [57–61].

Constant irradiation induces the formation and accumulation of defects in a crystals' atomic networks [57], and this will eventually result in the loss of long-range order in the network after sufficient energy has been absorbed. This is similar to what is observed in conventional glasses, where materials are quenched from the liquid state fast enough to avoid crystallization [1]. It is assumed that, after being exposed to a critical irradiation energy, the amount of defects will saturate and no further structural changes will be observed. However, it is unclear whether the effects of defect saturation are the same with the "state freezing" upon fast quenching in the MQ method. Similar to the vapor deposition and sol-gel glasses, in this thesis, we will evaluate the influences of irradiation on a crystal and assess the availability of the resulted glass.

Here, again via reactive molecular dynamics, we start with an α-quartz as an example mineral and demonstrate the impact of irradiation on crystal amorphization. By characterizing the different stability and structural features of the irradiated quartz, we will show that it is equivalent to a fast-quenched silica liquid.

2.3 Method

2.3.1 Melt-quenching

First, to set as references for all glasses mentioned in this chapter, we simulate the formation of bulk (for sol-gel condensation and irradiation) and freestanding film (for vapor deposition) forms of melt-quenched glassy silica [25]. First, initial configurations are created by randomly placing 512 SiO_2 molecules in a cube with lateral dimensions of 28 Å and periodic boundary conditions, while ensuring the absence of any unrealistic overlap. Second, the simulation boxes are fixed to 70 Å in the z-direction. Similar to the vapor deposition simulations, no periodic boundary conditions are applied along this direction and two reflective walls are placed on both ends of the simulation box. All systems are then relaxed at 3600 K and zero stress in the isothermal- isobaric ensemble (NPT) for 100 ps to ensure that they lose the memory of their initial configurations while nevertheless remaining a cohesive film. The obtained liquids are then subsequently quenched into glasses by linearly cooling the systems from 3600 to 300 K under zero stress in the NPT ensemble. Varying cooling rates ranging from 10,000 down to 1 K/ps are used to generate glasses exhibiting varying fictive temperatures [17], i.e., differing thermal histories. All glasses are eventually subjected to a zero-stress energy minimization to access their inherent configuration.

2.3.2 Vapor deposition

To establish our conclusions, we conduct a series of MD simulations of vapor-deposited SiO_2 glasses. A tetragonal simulation box with a height of 75 Å (z-axis) and lateral dimensions of 28 Å (x- and y-axis) is first created. The box is surrounded by two reflective walls on top and bottom, while periodic boundary conditions are imposed laterally. A melt-quenched silica glass with a vertical thickness of 14 Å is placed at the bottom and serves as substrate. The deposition process is then simulated by iteratively placing new SiO_2 molecules at the top of the box ($70 < z < 75$ Å) with a downward velocity of 0.02 Å/fs, wherein the initial horizontal position of inserted molecules is randomly chosen [15,44]. We find that a deposition rate of 0.5 SiO_2 /ps is slow enough to ensure a fair convergence of the potential energy of the deposited glass. Hence, this deposition rate is kept constant in all simulations. The substrate temperature used herein ranges from 500 to 3500 K—as we observe that, at higher temperature, the inserted particles remain in a gas phase and do not deposit on the substrate. The dynamics of all atoms is governed by a Langevin thermostat to model a Brownian dynamics during the deposition, wherein the temperature is controlled by adding some additional fictitious forces (friction and dispersion) [62]. We adopt this method since it has been shown to yield more stable vapor-deposited configurations than cases wherein the temperature of the vapor atoms is controlled by a Nosé-Hoover thermostat in the canonical ensemble (NVT) [15,44]. We use a damping factor of 50 fs and the rotational degrees of freedom are not thermostatted. The deposition process is continued until 512 SiO_2 molecules are deposited on the substrate, which results in the formation of a vapor- deposited glass that is about

35 Å high. The vapor-deposited configuration is eventually subjected to a zero-stress energy minimization using the conjugate gradient algorithm to obtain the inherent configuration [15,44,63]. This energy minimization under constant stress aims to remove any residual stress in the atomic structure but does not affect the connectivity of the glasses.

Note that, to filter out the effects of surface and substrate, we conduct all subsequent structural analysis on a subsection of the films that are far enough from the surface and substrate. The vertical extent of these domains (i.e., from z = 10-to-25 Å and z = 10- to-30 Å for the melt-quenched and vapor-deposited films, respectively) is determined by plotting some vertical profiles of the average potential energy per atom as a function of z. In each case, structural data are averaged over six independent simulations for statistical purposes. To ensure a consistent comparison between vapor-deposited and melt-quenched glasses, all simulations are conducted with the same forcefield. We adopt the reactive ReaxFF potential parameterized by Fogarty *et al.* [64], with a timestep of 0.5 fs which we would discuss more in detail in section . Importantly, ReaxFF can (i) account for charge transfers and dynamic formations of interatomic bonds [65], (ii) handle coordination defects [24,65], and (iii) realistically describe the structure of glassy SiO_2 [26]. Thanks to these features, ReaxFF can properly describe both the vapor deposition and melt-quenching processes with a constant set of parameters [66]. All simulations are conducted with LAMMPS [67].

2.3.3 Sol-gel condensation

We make the silica gel samples applying the same method introduced by Du et al [39]. and it could be broken down as the following steps: First, a group of $Si(OH)_4$ (orthosilicic acid) monomers are periodically distributed following a cubic lattice in a cubic simulation box with periodic boundary conditions. Next, some water molecules are randomly inserted in the remaining empty space in the simulation box while we apply some checking algorithms to ensure that there is no unrealistic overlap between the atoms. Here, we use H_2O/Si molar ratio = 3 that is shown to give the best dehydration result. A configurational demonstration is shown in Figure 2.3-1(a). Then the system is relaxed in the canonical (NVT) ensemble at 300 K for 100 ps using a Nose´–Hoover thermostat with a time constant of 25 fs. Following the NVT relaxation, the system is relaxed in an isothermal-isobaric (NPT) ensemble at 300 K and zero pressure for 250 ps with a Nose´–Hoover thermostat and a barostat time constant of 250 fs. According to Du *et al.* [39], this step allows the systems to shrink in order to help realize a zero pressure. The duration of this NVT-NPT combined relaxation is found to be long enough to ensure the convergence of both the potential energy and volume of the system. As shown in Figure 2.3-1(b), after the NVT and NPT relaxation, the $Si(OH)_4$ slightly reorganizes, but no condensation (i.e., formation of Si–O–Si bonds) is observed. This is associated with the high energy barriers of breaking of Si–O–H and formation of Si–O–Si bonds, which motivates us to apply an elevated temperature of 2000 K in the NVT ensemble for 1 ns. The result is shown in Figure 2.3-1(c) where it could be observed that some of the silicate monomers polymerize to form chains/rings.

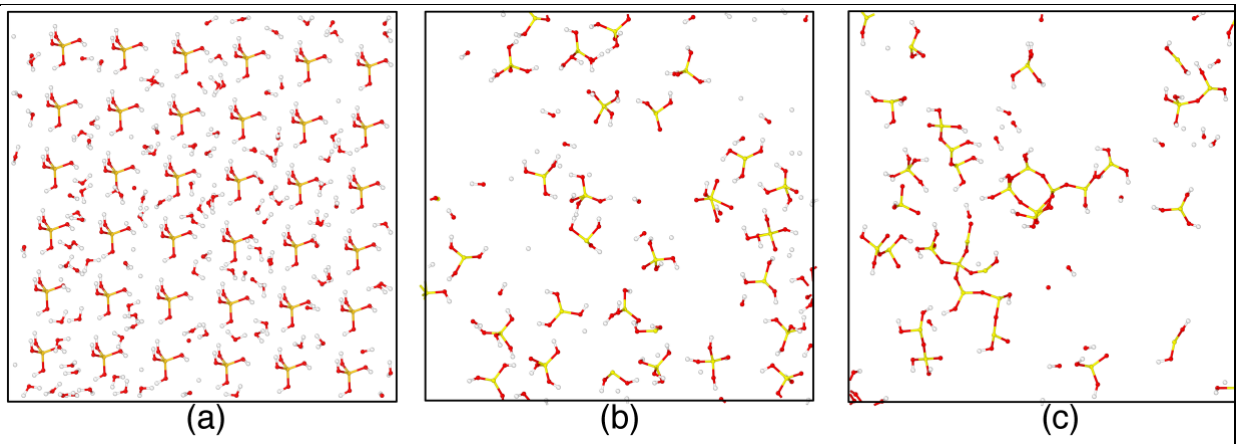

Figure 2.3-1

Slices of the atomic configurations of a SiO_2–H2O system obtained with ReaxFF-Fogarty obtained (a)after the initial construction of the configuration, (b) after the relaxation at 300 K, and (c) after 1 ns of reaction at 2000 K. Si, H, and O elements are represented in yellow, white, and red, respectively. Note that, in the panels (b) and (c), undissociated water molecules are omitted for clarity [39].

2.3.4 Irradiation

We carry out the realistic reactive MD simulations of irradiation-induced damage on a 10 × 10 × 9 α-quartz supercell with 8100 atoms using LAMMPS by following the well-established methodology from Krishnan et al [68–70]. First, a randomly chosen atom in the system is accelerated such that it is equivalent to being hit by incident neutron with the desired kinetic energy equal to 600 eV. Note that the probabilities are weighted based on the neutron cross

sections of silicon and oxygen atoms for a more accurate simulation. Once the atom is accelerated with the desired incident energy, it collides with other atoms to cause a ballistic cascade. A near spherical region is created around the impacted zone as a result, outside which atoms are kept at a constant temperature of 300 K by a Nosé-Hoover thermostat [71]. Similar to how we treat the incident SiO_2 molecule in the vapor deposition process, we model the dynamics of the atoms inside the sphere in an NVE ensemble to avoid any spurious effects of the cascade. The radius of the NVE sphere is fixed as 10 Å. Another thing to note that, a variable time step is used during the ballistic cascade to avoid potential numerical errors associated with the overlapping of atoms due to the high velocities of the primary and secondary knock-on atoms; a time step of 0.5 fs is used otherwise. The dynamics of the cascade is simulated for 20 ps, which was found to be long enough to ensure the convergence of both temperature and energy. Finally, every time following one collision, the system is further relaxed in the NPT ensemble at 300 K and zero pressure for another 5 ps for the system to adjust its density upon irradiation. This process is then repeated until the system exhibits a saturation in terms of both potential energy and density.

As already mentioned, because of the large spherical affected region that is created during each ballistic cascade, large system sizes are necessary to avoid potential spurious self-interactions arising from the periodic boundary conditions. Herein, we determine the system size by repeatedly knocking each atom of the quartz primitive cell, with the target radiation energy and in random directions. We then record the maximum distances traveled by each of the impacted atoms and choose the size of the system to be at least twice as large. This is why we make an

8100-atom supercell instead of the previously used 1536-atom cell in other methods. It is worth noting that, to offer realistic results, RMD simulations require the use of accurate interatomic potentials that can (1) correctly describe both the pristine and disordered structures of the relevant system with a fixed set of parameters, (2) provide a realistic description of high-energy collisions and (3) handle the formation of atomic species with defective local environments such as overcoordinated or undercoordinated atoms, which are likely to form upon irradiation. To this end, we choose the ReaxFF potential [65] with parameters taken from Manzano *et al.* [72], as it can correctly describe the structure of both pristine α-quartz and glassy silica especially in the sense that it can dynamically adjust the potential energy based on the local atomic environment of atoms [26]. Furthermore, thanks to the shielding of short-range interactions [22,73], ReaxFF can be used without any modifications to simulate high-energy collisions and ion bombardment.

2.3.5 Reaxff

As mentioned earlier, in this chapter, we simulate all the methods by relying on the ReaxFF reactive force-field that fits our simulation better than both AIMD and classical MD. ReaxFF is a bond order-based potential which has the advantage of accounting for the breakage and formation of chemical bonds that are the basis of chemical reactions. In ReaxFF, the total energy of the system E_{sys} is calculated through ten energy terms as follows [56,65]:

$$E_{sys} = E_{bond} + E_{VdWaals} + E_{Coulomb} + E_{under} + E_{over} + E_{lp} + E_{val} + E_{tors} + E_{conj} + E_{pen}$$

Equation 1

where the energy terms include, following the order above, the short-range bond energy, Van der Waals energy, Coulomb potential energy, under-coordination energy, over- coordination energy, long-range electron pairs energy, valence angle energy, torsion energy, conjugation energy, and penalty energy. The covalent terms (i.e., bond energy, valence energy, torsion energy, etc.) are derived continuously from a general relationship between the dynamic bond order and the interatomic distances and, hence, depend on the local environment of each atom. Additionally, unlike conventional classical force fields relying on constant charges, the charges of atoms are dynamically assigned based on a charge equilibration (QEq) method within the ReaxFF framework [74,75]. The partial charge of each atom depends on the atomic ionization potentials, atomic radii, and electron affinities. Altogether, thanks to these features, the ReaxFF force-field offers an ideal framework to simulate defected or disordered materials (i.e., thanks to its ability to adjust the energy terms based on the local environment of each atom) and the reactivity thereof (i.e., on account of its ability of model chemical reactions) [11,26,76]. All the simulations in this chapter are carried out with the Large-scale Atomic/Molecular Massively Parallel Simulator (LAMMPS) code while using the USER- REAXC package [67]. The velocity-Verlet integration algorithm is adopted to describe the motions of atoms with a time step of 0.25 fs. Note that several ReaxFF parametrizations are available in the literature for the Si–O–H system, including those developed by Fogarty *et al.*, Yeon *et al.*, and Deetz et al [51,64,77]. Based on

the results from Du *et al.* and our own observations, we find that the ReaxFF Fogarty potential offers the best performance and thus apply it in all simulated methods.

2.4 Result

2.4.1 Energy vs. volume

We now interrogate whether the glasses fabricated from the three methods are forbidden or allowable. That is, do they differ in nature from melt-quenched glasses, or can they also be formed by melt-quenching with a given (slow) cooling rate? To answer this question, Figure 2.4-1 shows the inherent structure average potential energy as a function of the average Voronoi volume per Q^4 Si atom in vapor-deposited glasses prepared with varying substrate temperature, the sol-gel glass, the irradiated-quartz and melt-quenched glasses prepared with cooling rates varying from 10000 to 0.1 K/ps (i.e., varying fictive temperature) [25]. To this end, rather than relying on the total potential energy of the system, we compute the potential energy per Q^4 Si atom (i.e., Si atom connected to four bridging oxygen atoms) to filter out the contribution of coordination defects and isolate the intrinsic thermodynamic stability of the network. Note that, as mentioned earlier, we also make a free-standing film version of melt-quenched glass for every cooling rate to ensure a fair comparison with the vapor deposition glasses. However, considering

the fact the average potential energy and atomic Voronoi volume only vary slightly and trivially between the bulk glass and the bulk part of film glasses, and for the sake of simplification, we are only showing the bulk melt-quenched glasses here. Similarly, for easiness of reading, we hide the error bars of each point in both directions but the range of the "banana-shaped" allowable region can approximately show the uncertainty of data of the melt-quenched glasses (e.g. the green region gets wider as the cooling rate increases because it is closer to a liquid state where atoms have higher kinetic energy to explore larger spaces and more thermodynamically unstable states). Although the potential energy and volume do not uniquely characterize a glass [78], the potential energy captures the degree of stability of a glass and, to the first order, largely depends on the short-range order, whereas the volume captures the overall compactness of the glass, which is strongly affected by the medium-range order [25]. As such, the energy-volume space shown in Figure 2.4-1 offers a convenient map to compare vapor-deposited and melt-quenched glasses.

We first focus on the melt-quenched glasses. For the range of cooling rates considered herein (which remain significantly larger than in typical experiments [25]), the average Voronoi volume per Q^4 Si atom decreases with the decrease in the cooling rate (i.e., the system becomes more optimally packed), while the average potential energy per Q^4 Si atom decreases and eventually plateaus (i.e., the system becomes more stable and achieves a lower fictive temperature) [25]. These states define the range of allowable states that are accessible to melt-quenched glasses within the time scale accessible to our MD simulations (i.e., as roughly indicated by the green region in Figure 2.4-1).

We now place our attention to the states occupied by vapor-deposited glasses in the energy-volume map. We find that, at high substrate temperature, vapor-deposited glasses are equivalent to hyperquenched melt-quenched glasses prepared with high cooling rates (see Figure 2.4-1). This signals that, in this regime, vapor-deposited glasses are allowable and the increase in potential energy upon increasing substrate temperature can be understood in terms of an increase in fictive temperature. This echoes the fact that, in this range of temperature, both vapor-deposited and melt-quenched glasses are able to relax toward the same metastable equilibrium super-cooled liquid state. In sharp contrast, at low substrate temperature, vapor-deposited glasses deviate from the states occupied by melt-quenched glasses in the energy-volume map (see Figure 2.4-1). Namely, upon decreasing substrate temperature, the potential energy per Q^4 Si atom increases while the volume per Q^4 Si atom keeps decreasing. This indicates that, in this regime, the increase in potential energy exhibited by vapor-deposited glasses upon increasing substrate temperature cannot be understood in terms of an increase in fictive temperature—so that such vapor-deposited glasses are forbidden. These results demonstrate that the allowable vs forbidden nature of vapor-deposited glasses depends on the substrate temperature.

Next, we find that the sol-gel glass appears at the left bottom corner of the map, indicating that it has an overall compact structure and is ultra stable compared to even the slowly quenched glasses. However, its Q^4 Si has a potential energy so low that the sol-gel glass clearly sits astray from where melt-quenching can reach on the map with slower cooling rate. This is an exciting discovery for it means that sol-gel condensation can potentially produce glasses that are more stable than common melt-quenched glasses requiring much lower temperature and time cost.

Last, the irradiated quartz is found to be well within the allowable region near the fast-quenching domain, which means that it is equivalent to a fast quenched silica liquid and should thus have similar properties. This agrees with the conclusion from Krishnan *et al.* [79] where they find that, though irradiation on crystalline quartz leads to forbidden disordered states at the initial stages, the system converges into the allowable region when the damage saturates.

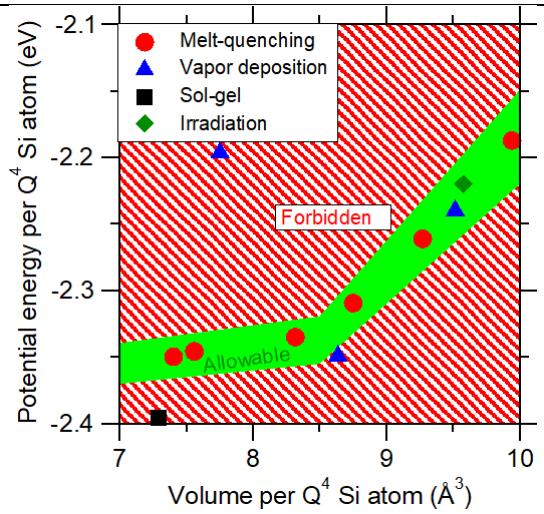

Figure 2.4-1

Inherent structure average potential energy as a function of the average Voronoi volume per Q^4 Si atom in (i) vapor-deposited glasses prepared with varying substrate temperature and (ii) melt-quenched glasses prepared with varying cooling rates (i.e., varying fictive temperature). The green region is a rough indication of the range of "allowable" states, whereas other states are "forbidden."

2.4.2 Nature of the forbidden glasses

From a first peek of the potential energy vs. Voronoi volume space, we find that:

1) The Allowability of vapor deposited glasses depend on the substrate temperature. They are allowable at high substrate temperatures that is supposed to be equivalent to melting silica liquid, but they become forbidden at low substrate temperatures in the sense that, though the entire structure becomes more compact, the glass is getting more unstable unlike melt-quenched glasses with low cooling rates.
2) The sol-gel glass is much more stable than the slowly quenched glasses of similar average atomic volumes and therefore appears to be forbidden.
3) Irradiation creates a glassy state that is the same with melt-quenched glasses with high cooling rates.

To understand why the forbidden glasses are forbidden, or the core mechanisms of how fabrication process can affect glasses' nature, we will delve deep into various structure-related features of vapor deposited and sol-gel glasses and explain their allowability from a bigger picture.

2.4.3 Atomic mobility in vapor deposition glasses

To understand the trend of allowability change in vapor deposited glasses, we first assess the thermodynamic stability of the vapor-deposited glasses as a function of the substrate

temperature. Figure 2.4-2 shows the inherent structure potential energy per Q^4 Si atom in vapor-deposited glasses as a function of the substrate temperature. The results are compared with the inherent structure potential energy of a melt-quenched freestanding glassy film prepared with a cooling rate of 1 K/ps [11,26,79]. Overall, we observe that the potential energy per Q^4 Si atom in vapor-deposited glasses exhibits a "V-shape" dependence on the substrate temperature, in agreement with previous results obtained for a 2D model glass [40,41]. The total potential energy per atom exhibits a similar trend (see the supplementary material). The most stable vapor-deposited glass is obtained for a substrate temperature of about 2500 K, which is slightly lower than the computed fictive temperature of the melt- quenched glass, that is, the temperature at which the energy exhibits a break in slope (see Figure 2.4-2)—note that both of these temperatures are here shifted toward higher values as compared to experiments due to the limited timescale accessible to MD simulations. This trend echoes previous simulation and experimental results [41,80]. Notably, at the substrate temperature of 2500 K, the vapor-deposited glass is slightly more stable than the melt-quenched glass—although this observation is specific to the deposition and cooling rates used herein. Overall, these results highlight that the behaviors of realistic (e.g., SiO_2) and model (e.g., Lennard-Jones) vapor- deposited glasses appear to be governed by the same underlying physics.

We now investigate the origin of the high stability featured by vapor deposited SiO_2 glasses at 2500 K (see Figure 2.4-2). In line with results obtained for 2D model glasses [44], we suggest that the mini- mum of potential energy arises from a competition between thermodynamics and kinetics. To establish this picture, we explore the dynamics of the vapor-deposited glasses by

computing the mean squared displacement (MSD) of the Si atoms as a function of temperature [80–83]. All calculations are conducted in the NVT ensemble over a duration of 250 ps. As expected, the MSD exhibits three stages, that is, (i) a ballistic regime at short time (slope of 2 in the log–log scale), (ii) a cage-effect plateau at intermediate time, and (iii) a diffusive regime, which manifests itself by a slope of 1 in the log–log scale [84,85] (see the inset of Figure 2.4-3). Notably, the dynamics of the surface atoms (i.e., within a 5 Å-thick region at the top of the sample) differs from those in the bulk. In detail, we find that the MSD of the surface atoms is systematically larger than in the bulk (see Figure 2.4-3)—albeit to a lesser extent at higher temperature. We also observe that the duration of the cage effect is about one order of magnitude shorter at the surface than in the bulk (see the inset of Figure 2.4-3). This likely arises from the fact that surface atoms are less constrained than bulk atoms [76] and, hence, have access to additional relaxation channels in the energy landscape [86].

Based on these results, the V-shape of the potential energy can be rationalized as follows [44]. At high temperature, the relaxation time of both vapor-deposited and melt-quenched systems is smaller than the observation time. Hence, both systems can reach the metastable equilibrium supercooled liquid state. As temperature decreases, lower-energy supercooled liquid states become more thermodynamically favored, so that both vapor-deposited and melt-quenched systems reach more stable positions in the energy landscape. However, at the vicinity of the glass transition, due to the kinetics slowdown, the relaxation time of bulk melt-quenched systems becomes longer than the observation time—so that they become out- of-equilibrium glasses and remain stuck in unstable positions in the energy landscape. In contrast, at constant observation

time, vapor- deposited glasses relax faster than melt-quenched glasses, thanks to the faster kinetics of their surface atoms. Hence, vapor-deposited glasses remain in the metastable equilibrium supercooled liquid state down to lower temperatures (and, hence, reach more stable basins in the energy landscape) than melt-quenched glasses at constant observation time. However, as the substrate temperature continues to decrease, the increased slowdown in relaxation kinetics eventually prevents the atoms from relaxing toward low-energy states when they get deposited at the glass surface, which results in an increase in potential energy. Overall, the substrate temperature at which vapor- deposited glasses feature minimum potential energy is controlled by the competition between thermodynamics (i.e., increased thermodynamic propensity to relax toward lower-energy states as temperature decreases) and kinetics (i.e., decreased ability to reach such stable states as temperature decreases).

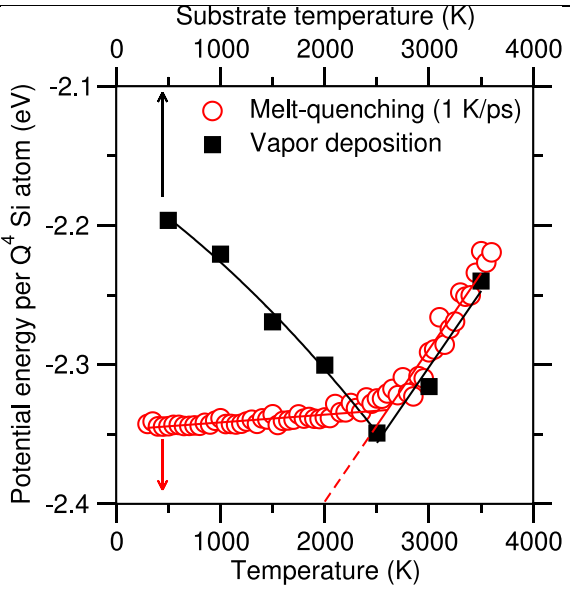

Figure 2.4-2

Inherent structure average potential energy per Q^4 Si atom in both (i) vapor-deposited glasses as a function of the temperature of the substrate and (ii) a melt-quenched glass prepared with a cooling rate of 1 K/ps as a function of temperature. In each case, the arrows point toward the relevant temperature to be considered. The solid lines are to guide the eye. The dashed line is an extrapolation of the supercooled liquid domain.

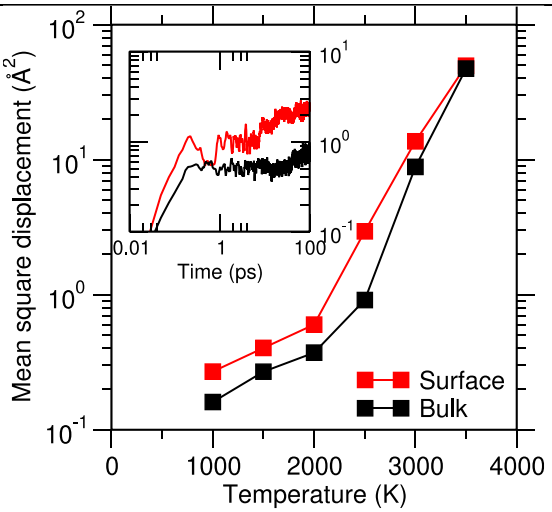

Figure 2.4-3

Mean squared displacement (MSD) after 250 ps of dynamics of Si atoms located in the bulk or surface of vapor-deposited SiO_2 glasses as a function of temperature. The inset shows the MSD for bulk and surface Si atoms at 2500 K.

2.4.4 Ring-size distribution

Though now we know that the way substrate temperatures determine the stability of vapor deposited glasses is based on the competition of dynamics and kinetics, this does not explain the trend of their allowability changes. To approach this, we now draw our attention to the structural features. Note that, in the following, to ensure a fair comparison between the atomic structure of vapor-deposited and melt-quenched glassy films, we restrict the comparison to glasses having

fairly similar potential energy (see Figure 2.4-2 for a comparison between the energy of vapor-deposited and melt-quenched glasses). In detail, we conduct three distinct comparisons: (i) the "forbidden" sol-gel glass is compared with a melt-quenched glasses cooled at 0.1 K/ps, (ii) the "forbidden" vapor-deposited associated with a substrate temperature of 500 K is compared with a melt-quenched glassy film cooled at 10000 K/ps, and (iii) the "allowable" irradiated-quartz is compared with a melt-quenched glassy film cooled at 10000 K/ps.

To begin, we find that regardless of the fabrication method, the Si–O partial pair distribution functions obtained from the three cases and melt-quenched glasses match well with each other (see the supplementary material). Similarly, the O–Si–O intra-tetrahedral partial bond angle distributions do not reveal any notable differences between the short-range order structure of both glasses either (see the supplementary material). This may partially explain why vapor-deposited glasses have previously been assumed to be structurally similar to melt-quenched ones [44]. The short-range order analysis being largely inconclusive, we change our focus to the medium-range order, which, in silicate glasses, is described by the ring size distribution [87–90]— wherein a ring is defined as a closed path made of Si–O bonds in the network with a size being given by the number of Si atoms. All ring size distributions are computed using RINGS [89]. Figure 2.4-4 shows the ring size distribution of the three selected vapor-deposited glasses, which, in each case, is compared to that of their melt-quenched counterparts. For simplicity, we do not show the other vapor deposited glasses here since the allowable ones all have similar distribution with the case of irradiation and the forbidden ones can be well represented by the 500 K sample. We find that, as expected, all distributions are centered around 5–6 membered rings [10]. We first

note that no significant difference is observed between the ring size distribution of the "allowable" vapor-deposited glasses and the irradiation glass (i.e., at high and intermediate substrate temperature) and that of their melt-quenched counterparts [see Figure 2.4-4(b) and (c)]. However, in contrast, we observe that the ring size distribution of forbidden vapor-deposited glasses (i.e., prepared with low substrate temperatures) exhibit distinct features. In detail, we find that the ring size distribution of the forbidden vapor-deposited glass presents an excess of small rings (i.e., 4-membered rings and smaller) as compared to its melt-quenched counterpart, as well as in comparison to the other allowable vapor-deposited glasses [see Figure 2.4-4(a)]. Such small rings have been shown to be topologically over-constrained and to constitute a signature of instability [10,87]. Such instability manifests itself by a decrease in the average value of the inter-tetrahedral Si–O–Si angles (see the supplementary material), which echoes previous findings [10]. In turn, such small rings result in the formation of efficiently-packed structures—since small rings are associated with low diameters, whereas larger rings present more open structures.40 As such, the existence of a large fraction of small rings explains why forbidden vapor-deposited glasses prepared with low substrate temperatures simultaneously exhibit high potential energy and high packing efficiency. Such small rings can be formed when atoms get randomly deposited at the surface of the glass—irrespective of the substrate temperature. However, due to their unstable nature, small rings are likely to quickly disappear as the surface atoms relax toward more stable configurations. However, the slowdown in relaxation kinetics experienced by vapor-deposited glasses prepared with low-temperature substrates prevents the efficient relaxation of such energetically unfavorable small rings.

We note that the excess of unusual small rings observed herein at low substrate temperatures echoes previous observations of local molecular anisotropy in vapor-deposited glasses [43,91,92]. Indeed, in both cases, such unusual structural features (i.e., small rings in network glasses or anisotropic molecular orientation in molecular glasses) are formed at the glass surface upon deposition and, if relaxation is slow enough, remain trapped within the bulk after further deposition occurs. In both cases, the propensity to retain such unusual structural features frozen within the bulk increases as the deposition temperature becomes lower as compared to Tg due to the dramatic slowdown of the relaxation kinetics. In turn, when the deposition temperature exceeds Tg, the existence of fast relaxation modes prevents the accumulation and persistence of such defected structural features.

Lastly, we observe that, though the sol-gel glass has slightly more large rings than a slowly quenched glass, their ring-size distributions are, overall, quite similar. Moreover, large rings do not necessarily lead to averagely more stable states (e.g. a fast quenched silica glass has significantly more large rings than a slowly quenched one but higher potential energy at the same time), which means that only the ring size itself may not be enough to explain the extra stability possess by the sol-gel glass. This drives us to assess ring properties from other aspects, say, the shape of the ring.

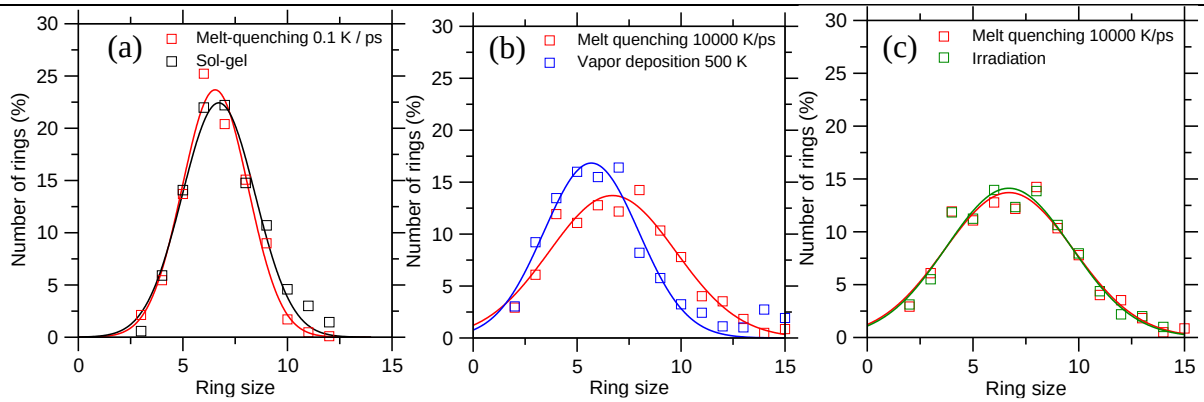

Figure 2.4-4

Ring size distribution in glasses made from the process of (a) sol-gel condensation, (b) vapor deposition with substrate temperature at 500 K, and (c) irradiation. In each of these cases, the distributions are compared with those obtained in a melt-quenched glass presenting a molar potential energy that is comparable with that of the target glass (i.e., as obtained with a cooling rate of 1 K/ps, 10000 K/ps, and 10000 K/ps, respectively). The lines are to guide the eye.

2.4.5 Shape of rings

There are many ways to describe the shapes of rings. Here, we apply the concept of ring eccentricity that is defined as:

$$e = \sqrt{1 - \frac{b^2}{a^2}}$$

Equation 2

where a > b with a, b being the longest and shortest distance from the geometrical center to any Si atom in the ring. This is the same with its original definition that describes how round or how elliptical a semispherical object is. The reason why we manage to simulate this property is because, based on the results from ring-size distribution, the motional modes possessed by the atoms in a ring as a whole may be different between two rings even with them being of identical sizes. That is, a more elliptical ring has extra floppy modes that may contribute to the atoms' exploration to more stable states, while round rings do not. The measured average eccentricity vs. average ring size is shown in Figure 2.4-5.

First, we see that the melt-quenched silica forms a straight allowable region across the map from top right to bottom left. This agrees with what we expect because, in the same way a fast quenched melt have more small rings, it can also have a much higher number of large rings, which are usually elliptical rather than round, due to the "locking" of some thermodynamically unfavored unstable states. While a slowly quenched glass will have mostly just 6-membered rings that are isostatic thus more inclined to be round. This can be seen from Figure 2.4-4 if we compare the ring-size distribution of melt-quenched glasses with high and low cooling rates. Additionally, as expected, the irradiated-quartz and vapor deposited glasses associated with high substrate temperatures fall in the allowable region again.

Next, we find that the vapor deposited glass of substrate temperature equal to 500 K appears below the allowable region, which means, compared to melt-quenched glasses with similar average ring sizes, its rings are rounder. This echoes with our findings in the previous section where it has a larger fraction of small rings which tend to be round. This is because a ring with

fewer atoms must change its interatomic angles by a larger degree if its atoms would change its position relative to the other atoms than under the same situation in a larger ring, and this means higher energy barriers to overcome thus harder for it to be elliptical.

Finally, the sol-gel glass is located towards the left top of the allowable region meaning it exhibit an excess of flexible elliptic rings that, based on our former derivations, can buckle to facilitate the relaxation of the glass toward more stable structures. Now we may preliminarily conclude that, the floppy modes arising from the elliptic shape of the rings is what enable the sol-gel glass to become more stable than a melt-quench glass. Moreover, the elliptic shape of the rings forming upon sol-gel condensation process is a consequence of the fact that rings have to be deformed as the connect to each other upon drying. Additionally, the distorted network connections will also contribute to the creation of a large number of voids and pores observed by Du *et al.* [39]

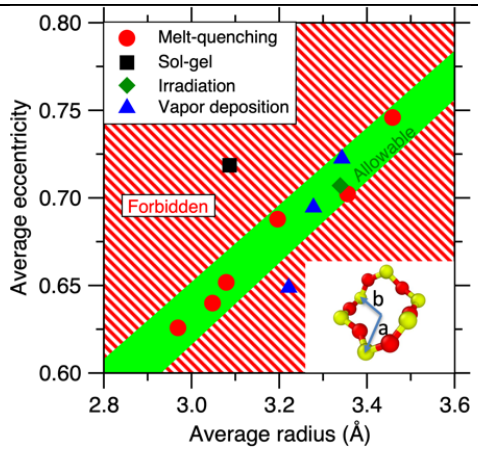

Figure 2.4-5

Average ring eccentricity as a function of the average ring radius in: vapor-deposited glasses prepared with varying substrate temperature, the sol-gel glass, and irradiated-quartz. The green region is a rough indication of the range of "allowable" states depicted by the melt-quenched glasses of different cooling rates (from left bottom to top right: higher cooling rates), whereas other states are "forbidden." The inset is a configurational silica ring showing the definition of the longest (a) and shortest (b) radius.

2.4.6 The energy landscape– the bigger picture

We now ascend to a higher viewpoint to show the energy landscape as a summary to this chapter to illustrate the different regions of the energy landscape explored by different synthesis methods and how this will affect all the other properties we have observed and compared thus far.

For this purpose, only having the average atomic potential energy is not enough to draw the configurational picture of energy – states distribution, and it is necessary to also calculate the interatomic energy barrier, which can quantify the general propensity of the glass atoms to converge towards thermodynamically more favored stable states. To this end, we apply the activation-relaxation technique (ART) [93,94] whose working mechanisms can be summarized as the following: first, based on the initial system, an altered configuration is activated from a local minimum to a nearby saddle point; next, the configuration is relaxed to a new minimum; this allows for jumps over energy barriers much higher than what can be reached with standard simulation techniques and will thus help sample the energy barriers between any atoms. Figure 2.4-6(a) lists the normalized ART-calculated energy barrier distribution of the melt-quenched and forbidden glasses where we can divide the histogram into two major modes using the same way Fan *et al.* [95] propose in their discussion of metallic glasses: 1) a low energy exponential decay mode and 2) a shifted-Rayleigh distribution. They interpret these two modes as to be correlated with the atomic state changes where there aren't breaking of chemical bonds (mode 1) and where there are (mode 2), separately. We are especially interested in the former because this is essentially equivalent to the floppy modes provided by the silica rings, and the magnitude of this exponential curve is thus strongly correlated with the richness of such modes. We fit the exponential decay mode using the following expression:

$$P = W \cdot \frac{1}{\varepsilon_A} \exp\left[-\frac{E_A}{\varepsilon_A}\right]$$

Equation 3

where p is the probability distribution function (PDF), E_A is the activation function (a.k.a. energy barrier), ε_A is a material-dependent average activation energy that, in the case of SiO_2 glass, we choose to be 0.5 eV [95], and W is the magnitude. Since the distribution is already normalized for all glasses, we use a non-linear fitting algorithm to get the value of W and fitted exponential curve is shown as an orange line on top of each distribution. Note that, since the floppy modes are only associated with low energy values (typically < 2 eV) [87,95,96], we will use 2 eV as a threshold for the fitting and ignoring the distribution at higher energy barriers.

In Figure 2.4-6(e) we show the calculated W values with their corresponding average potential energies for all glasses. We first find that, as a general trend, the glasses that show higher eccentricity in Figure 2.4-5 also have higher W values. This validates our previous argument that the more elliptical rings a simulated glass has tend to enrich the floppy modes in the networks which is once again captured by energy barrier calculations. Specifically, about each glass, the number of low energy ring floppy modes in a melt-quenched silica increases with higher cooling rates, meanwhile the low substrate temperature vapor deposition and sol-gel process leads to fewer and more of these modes separately compared with their melt-quenched counterparts with similar stability.

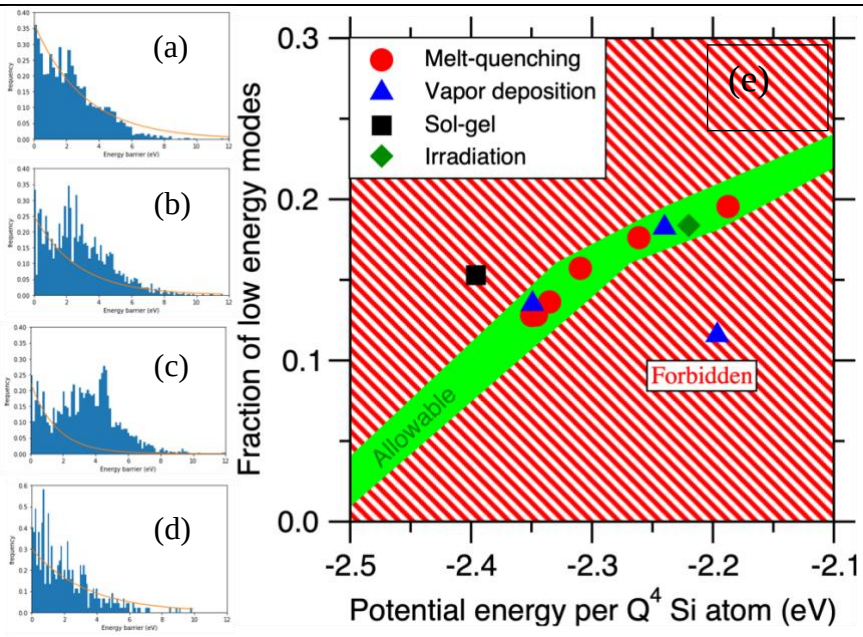

Figure 2.4-6

The interatomic energy barrier distribution of glasses made from (a) melt-quenching with cooling rate 10000 K/ps, (b) melt-quenching with cooling rate 0.1 K/ps, (c) vapor deposition with substrate temperature 500 K, and (d) the sol-gel process. The orange lines indicate the fitted exponential decay modes. (e) The fitted magnitude of the exponential decay modes of all glasses. From left bottom to right top: melt-quenching with increasing cooling rates. Vapor deposition: top middle: substrate temperature 3500 K, left: 2500 K, bottom right: 500 K.

2.5 Conclusion

Finally, as the conclusion of this chapter, we are able to draw the configurational energy landscape using all the information about energy and states that we have collected so far, which is shown in Figure 2.5-1.

Starting from the left, we can now comment on the allowability of each glass based on their stability, and their energy barriers associated with ring floppy modes that is a collective demonstration of their structural flexibility and network medium-range order:

1) The sol-gel process produces a highly stable glass with a large fraction of elliptical rings. The excess of such flexible rings enables the relaxation of the glass towards more stable thermodynamic states at the same level of compactness and average ring sizes compared to even the slow quenched glass, which makes it a forbidden glass. Moreover, the distorted connection between silica tetrahedrons resulting from the drying process may lead to nonuniformity of atomic distribution in the network, creating dense areas and voids at the same time.
2) The irradiation process, after the saturation of the irradiation-induced damage, will make a quartz crystal equivalent to a glass made by quenching a silica liquid with high cooling rate, which is a glass that is unstable and having low energy barriers among atoms.
3) The forbidden or allowable nature of vapor-deposited glasses depends on the temperature of the substrate used during deposition and is controlled by a competition between thermodynamics and kinetics—wherein thermodynamics drives the relaxation of vapor-

deposited glasses toward allowable metastable supercooled liquids, whereas kinetics can prevent such relaxation and tend to freeze some unrealistic small ring defects formed during deposition that are unstable, highly rigid, and otherwise virtually absent from allowable melt-quenched glasses. Lastly, the fact that both the melt-quenched freestanding films and vapor-deposited glasses present a free surface ensures that differences in the structure and properties of melt-quenched and vapor-deposited glasses are not just a spurious consequence of the presence of a surface.

More generally, these results suggest that the allowable vs forbidden nature of disordered networks is encoded in their medium-range (rather than short-range) order. These results also suggest that, in addition to being a promising route toward the synthesis of ultrastable allowable glasses (e.g. sol-gel process, vapor deposition near at the substrate temperature near the glass transition temperature), the methods discussed in this chapter may offer an intriguing pathway toward the design of forbidden glasses that are not accessible to the melt-quench route and, hence, could exhibit unusual properties (e.g., enhanced mechanical properties and low propensity for relaxation).

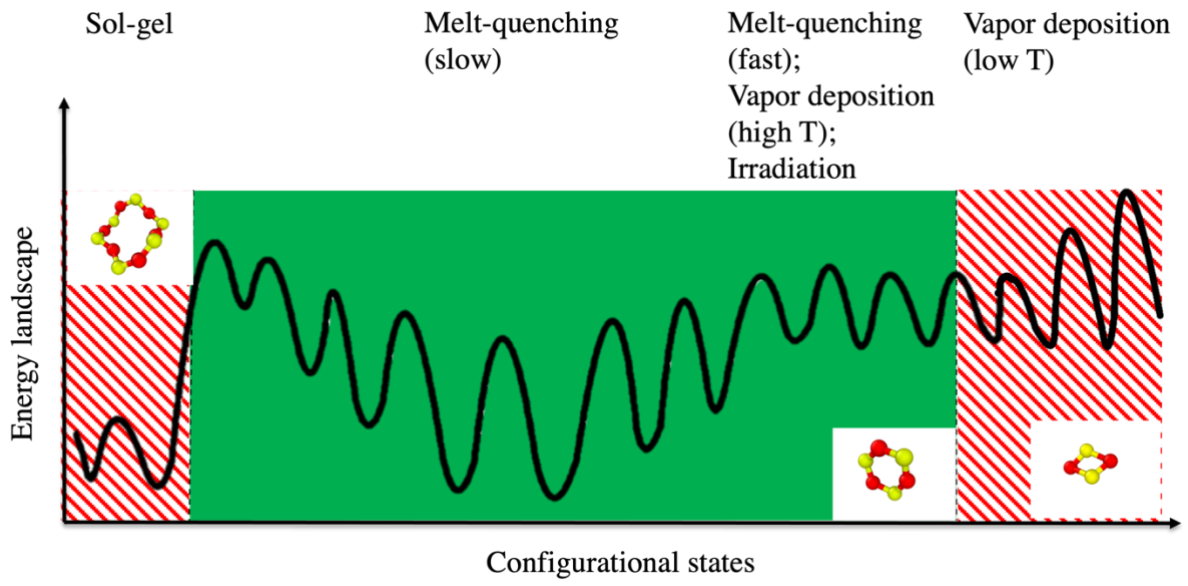

Figure 2.5-1

The configurational energy landscape of all the glasses mentioned in this chapter could be divided into 3 regions: 1) the forbidden sol-gel glass, 2) the allowable region, including the irradiated quartz and vapor deposited glasses with high substrate temperatures, and 3) the forbidden low-substrate temperature vapor deposited glass. The relative height of each wave packet symbolizes the inherent potential energy, and its magnitude shows the magnitude of energy barriers. The inset plots show characteristic rings of each region.

3 Chapter II Decoding zeolite crystallization and stage III in nuclear waste glasses by coupled modeling

3.1 Overview of this chapter

Based on the presumption that the stage III in nuclear waste glasses is thought to be closely related to the precipitation of zeolites, this chapter aims to investigate the thermodynamic propensity for zeolite formation and the kinetic motivation as a function of solution conditions. To reach this goal, this chapter will go through three steps:

1) Goal of this part is to use *ab initio* molecular dynamics (AIMD) to calculate the thermodynamic properties (including formation enthalpies, standard molar entropy, and isobaric heat capacity) for a group of characteristic zeolites, which features many cation compositions, various hydration levels, a wide range of frameworks and may contain partial atomic site occupancies. We will first give a detailed demonstration of the theoretical bases and simulation method, then show that our method offers accurate results by comparing them with existing experimental data.
2) Based on the thermodynamic data of over 20 types of common zeolites that we collect using the methodology we derived in step1, we build a preliminary database and use Gibbs Energy Minimization (GEM) to model zeolite stability under various solution conditions (solution composition, pH and temperature). We will give a brief introduction of the GEM Selektor (GEMS) software interface, its working principles and how it plays its role in our cause. We then compare the stability fields and precipitation mapping of various zeolites that we get from GEMS and validate them using experimental data.

3) At last, using the results we get from step 2 both as training and testing data, we build a machine learning model that can accurately predict the precipitation of zeolite based on any input solution parameters.

Basically, steps 1 and 2 are unending data-harvesting processes that will continue to benefit their next steps as long as more accurate data is obtained. Especially for step 3, ML models typically require thousands of data or even more for the best learning and predicting results on complex relationships, which means that this thesis is far from concluding on getting an ideal model and more work will always improve it in the future.

Moreover, we will describe some interesting findings on the simulation of zeolitic water, the way it may contribute to the volume-based thermodynamics of zeolites and similar boro(alumino)silicate-based crystals, and an analysis on the impacts of various features on zeolite precipitation based on the results we get from our machine learning model.

3.2 High-throughput simulation of zeolite phases

As the first step of this chapter, obtaining accurate thermodynamic data of zeolites is crucial in predicting their formation conditions. However, the present lack of thermodynamic data for zeolites (especially for defected and/or partially hydrated phases) makes it challenging to predict their propensity to precipitate as a function of pH and temperature. This presently limits our ability to accurately predict the long-term dissolution kinetics of nuclear waste immobilization

glasses. Here, we investigate the thermodynamic properties of a collection of simple zeolitic phases by high-throughput ab initio molecular dynamics simulations. We show that the simulated data exhibit a very good agreement with experimental data, when available. Based on these simulations, we propose a series of analytical models enabling the prediction of zeolite's thermodynamic properties based on their composition and structure.

3.2.1 Methods

We first focus on a total of eight zeolites, namely: analcime [97–99], natrolite (Sodium) [100]; wairakite [101], scolecite [100], laumontite [101], leonhardite [101], yugawaralite (Calcium) [101]; and K-phillipsite (Potassium) [102,103]. We choose these zeolites based on following reasons: (1) They possess relatively simple unit-cell structures. Yugawaralite, which has the most atoms among the eight, only has 50 atoms in one unit-cell. Due to the restriction of *ab initio* simulations on system sizes, which is typically on the level of hundreds of atoms, a smaller unit-cell means more cells in the simulation box, which increases periodicity and accuracy. (2) Atoms in these zeolites don't have partial occupancies. Zeolitic cations and water molecules characteristically tend to have partial occupancies in zeolite frameworks, that is, they are not guaranteed to appear at their sites in every unit-cell, which is shown in many experimental data [100,104–107]. Inevitably, this brings immense difficulties for molecular dynamic simulations where only systems that comprises a fixed atomic configuration at the same time could be modeled. One way to tackle this problem is to increase the system size until the numbers of all types of atoms are integers, but this often simultaneously raises the required computational efforts way beyond the limit of *ab initio*

simulation [108]. We will discuss more on this topic in 3.2.2.5 where we propose a linear-combination method to try to approach this problem, but, here, only use simpler zeolites for the development of the basic methodology. (3) They are common zeolites that appear in many fields such as catalysis and nuclear waste immobilization glasses, which has abundant experimental records, especially room-temperature data [97,100,101,104]. (4) They cover most of the common network modifiers in alumina-silicate, namely, sodium, calcium and potassium. By looking at the properties of zeolites with the same framework but different modifiers (e.g. analcime (cation: Na) and wairakite (cation: Ca)), we are able to evaluate the difference these cations bring to their thermodynamics.

We use the Vienna *Ab Initio* Package (VASP) [18,109–111] and the Phonopy package [112] for all the *ab initio* simulations in this chapter. We select the Perdew, Burke and Ernzerhof (PBE) functional [113,114], which was proven to be effective in dealing with alumina-silicate materials. The initial configurations of the zeolite systems are sourced from the International Zeolite Association (IZA) Structure Commission database [115], and all other materials (single element phases, oxides, etc.) that are used in the calculation of zeolite properties are referenced from the Materials Project [116]. The atomic cell is first relaxed with an ionic relaxation process based on the conjugate gradient algorithm (VASP code IBRION=2) for 100 fs. Then, the system undergoes a subsequent MD relaxation under NPT ensemble of 500 fs at 300 K—which was found to be long enough to obtain a convergence of the energy. We apply the ionic relaxation instead of purely relying on the room-temperature MD simulation for this can dramatically reduce the total relaxation time and can

eventually yield a similar level of convergence in total energy. For all *ab initio* calculations, the energy cutoff is set as 520 eV and the timestep is fixed kept at 0.5 fs. The total energy of the system is then obtained by averaging the instantaneous energy after convergence is achieved. The K-point grid is automatically generated using the gamma-centered scheme with 11 subdivisions along each lattice, with the exception of calculations for oxygen that used a Monkhorst-Pack grid.

We also apply classical MD in this work for longer time-scale simulations, which is necessary in scenarios like capturing the rotational motion of zeolitic water molecules. For classical MD, we rely on Lammps [67] and the reactive ReaxFF Pitman forcefield [117], which offers a realistic description of silicate-based crystals. We choose a timestep of 0.5 fs, which is consistent with *ab initio* simulations. And all classical simulations are carried out based on the relaxed zeolite configurations from *ab initio* simulations for a maximized accuracy.

3.2.1.1 Molar volume and density

First, we simulate the molar volume of chosen zeolites. This can be directly calculated by carrying out a relaxation of the zeolite framework under NPT ensemble at 300 K using VASP (VASP code IBRION=0 for molecular dynamics, and ISIF=3 to relax atomic positions, cell shapes and volumes), and by doing a statistical average while the cell volume starts to converge. 500 fs is found to be sufficient to observe such convergence for all simulated zeolites. The density is accordingly obtained by considering the masses of atoms in the unit cell.

3.2.1.2 Formation enthalpy

To calculate the formation enthalpy of zeolites, we consider the following reference elemental systems: (i) body- centered cubic Na (sodium), (ii) face-centered cubic Al (aluminum), (iii) face-centered diamond- cubic Si (silicon), and (iv) gas phase O (oxygen) (v)Ca (vi)K. The formation enthalpy of each oxide system A_xB_y is then computed as the reaction enthalpy ($\Delta_r H$) associated with the reaction xA + yB = A_xB_y as:

$$\Delta_r H = H_{AxBy} - (x\ H_A + y\ H_B)$$

Equation 4

where H is the enthalpy of each system.

As an example, the formation enthalpy of analcime ($\Delta_f H_{\text{ana}}$) based on its compositional elements is shown by the following equation:

$$\Delta_f H_{\text{ana}} = E_{\text{ana}} - E_{\text{Na}} - E_{\text{Al}} - 2 \cdot E_{\text{Si}} - 7 \cdot E_{\text{O}}^{\text{corrected}} - 2 \cdot E_{\text{H}}^{\text{corrected}}$$

Equation 5

where E_{ana} is the total energy of analcime, E_{Na}, E_{Al}, and E_{Si} are the enthalpies of formation of individual elements, and $E_{\text{O}}^{\text{corrected}}$ and $E_{\text{H}}^{\text{corrected}}$ are the corrected energies for O_2 and H_2., respectively. Note that we use corrected energy terms for oxygen (O_2, 4.23 eV per O) and hydrogen

(H_2, 3.6 eV per H), as suggested by Materialsproject and Pymatgen [116,118]. These corrections are found to be necessary to overcome the limitations of the generalized-gradient approximation for gaseous reactants. To evaluate the uncertainties, we divide the converged area of energy-time curve into 10 equal periods and calculate the average and standard deviation values based on the data from these parts.

3.2.1.3 Entropy

To calculate the entropy using *ab initio* methods, we apply the Phonopy package. Here, our primary hypothesis is that, in the crystalline phases considered herein, entropy solely arises from the vibrational degree of freedom. As such, due to the crystalline nature of dehydrated zeolites, we ignore the rotational and translational contributions to the entropy [112,119]. To calculate the vibrational entropy, we map the dispersion relation (i.e., the relationship between the phonon frequency ω and wave vector q) by applying the Parlinski-Li-Kawazoe (PLK) method implemented in Phonopy, which is a numerical fitting approach to obtain the force constants from forces and displacements [120,121]. After calculating the force constant matrix, the dispersion relationship for each vibration mode can be numerically solved with lattice dynamic theories [122]. The relationship between the interatomic forces (i.e., first derivatives of the interatomic potential) and the Hessian matrix (i.e., second derivatives of the interatomic potential) is given by:

$$\boldsymbol{F} = -\boldsymbol{UP}$$

Equation 6

where $\boldsymbol{F}$, $\boldsymbol{P}$, and $\boldsymbol{U}$ are the forces, Hessian matrix, and the atomic displacement, respecively. Here, according to the PLK method, we intentionally vary $\boldsymbol{U}$ based on the lattice symmetry to get a set of displaced lattices. In the case of dehydrated analcime, 120 displaced configurations are generated. $\boldsymbol{F}$ and $\boldsymbol{P}$ are then calculated by VASP using the command IBRION = 8 for each sample with different values of $\boldsymbol{U}$. The energy cutoff is kept at 520 eV, which is consistent with the number used during the initial relaxation. Finally, we use Phonopy to fit the results corresponding to each value of $\boldsymbol{U}$ and compute the approximated matrix of force constant Φ, that is, a numerical fitted estimation of P. It is worth mentioning that, to ensure that the chosen lattice is big enough to demonstrate periodicity and feature a sufficiently large pool of $\boldsymbol{U}$ values, an empirical enlargement is sometimes applied to the original lattice to make it a supercell—with volumes larger than 1000 $Å^3$. For example, the original reference SiO_2 unit cell is here found to be too small and, hence, a 2x2x2 superlattice is used for the entropy calculation. However, the analcime sample is not changed as its unit cell size is found to be large enough.

After obtaining the matrix of force constant Φ, we calculate the dispersion relation based on the harmonic approximation (HA) [122], which assumes that the near-range vibration of an atom around its equilibrium position can be treated as a harmonic oscillator, that is, its displacement can be simply written in a plane-wave fashion as:

$$u_{j,\alpha} = \varepsilon_{j,\alpha}(\boldsymbol{q})\exp(i\boldsymbol{q}\cdot\boldsymbol{r} - \omega(\boldsymbol{q})t)$$

Equation 7

where ε is the polarization vector, j and α denote the complex and real space Cartesian directions (x, y, z), respectively, r is real space equilibrium position, and ω is the angular phonon frequency. This yields the eigenvalue equation:

$$D_{\alpha\beta}^{jj'}(\boldsymbol{q})u_{j,\alpha} = \omega(\boldsymbol{q})^2 u_{j,\alpha}$$

Equation 8

Where

$$D_{\alpha\beta}^{jj'}(\boldsymbol{q}) = \frac{1}{\sqrt{m_j m_j'}}\sum_{l'}\Phi_{\alpha\beta}(0,j;l',j')\exp\left(i\boldsymbol{q}\cdot[\boldsymbol{r}(j',l') - \boldsymbol{r}(j,0)]\right)$$

Equation 9

is the dynamical matrix expressed in the PLK theory or the mass-reduced Fourier transform of Φ. Here, m is the atomic mass, and l is the index of each repeated unit cells. The sum over l is performed to consider the atoms from all neighboring cells. The dynamical matrix is then obtained based on the calculated Φ and Phonopy is able to numerically solve the eigenvalue equation to yield the dispersion relation for desired phonon modes. The partition function can be calculated by summing all these modes, which, in turn, can be used to calculate some thermodynamic properties based on statistical mechanics, e.g., the constant volume heat capacity or the Helmholtz

free energy. In particular, the entropy can be obtained from the derivative of the Helmholtz free energy with respect to the temperature T:

$$S = \frac{\partial F}{\partial T} = \frac{1}{2T}\sum_{\boldsymbol{q}} \hbar\omega(\boldsymbol{q}) \coth\left(\frac{\hbar\omega(\boldsymbol{q})}{2k_{\mathrm{B}}T}\right) - k_{\mathrm{B}}\sum_{\boldsymbol{q}} \ln\left[2\sinh\left(\hbar\omega(\boldsymbol{q})/2k_{\mathrm{B}}T\right)\right]$$

Equation 10

where k_{B} is the Boltzmann constant.

All phonon calculations are based on the harmonic approximation and thus fully volume-independent. To calculate volume-dependent thermodynamic properties such as the isobaric heat capacity, thermal expansion coefficient, and bulk modulus, etc., we adopt the quasi-harmonic approximation (QHA), which takes into account the change of volume [119]. This is simply done by expanding or shrinking the unit-cell and repeating the aforementioned workflow for each new volume V. In our case, we vary the volume from 95% to 105% of that of the original lattice. For the Phonopy calculation does not provide uncertainties by itself, we thus, for each case, randomly pick three configurations out of the relaxed MD periods and do the same simulations.

However, Phonopy does not offer an ideal prediction of the entropy of hydrated zeolites, as will be discussed with more details in the 3.2.2 result section. The reason is that, unlike the lattice atoms, only considering the vibration of zeolitic water molecules is not enough to describe its complete motion where rotations must also be included for accurate calculation of the entropy.

Describing the rotational motion of a water molecule in a given crystal lattice requires the definition of three angles (Figure 3.2-1): (i) theta, which describes the altitudinal orientation of the dipole (ranging from 0 to π), (ii) phi, which describes the azimuthal orientation of the dipole (ranging from 0 to 2π), and (iii) beta, which describes the rotation of the two hydrogen atoms around the dipole (ranging from 0 to π based on C_{2v} symmetry). The angles must be defined based on a reference plane, which, here, is defined as the plane that comprises the central O of the water molecule and the two nearest framework cations. The distribution of these three angles can be obtained by tracking the motion of the water molecules over time [123].

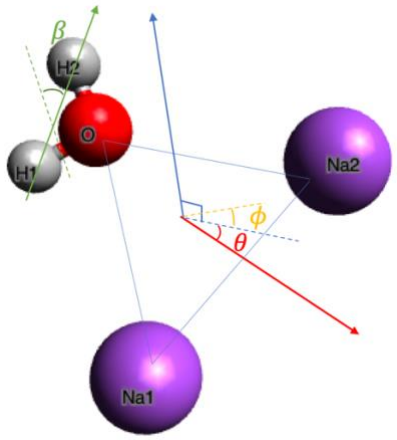

Figure 3.2-1

Illustration of the three angles defining the orientation of water molecules in zeolites (using here the example of analcime). The red arrow represents the direction of the dipole moment of the water molecule. The blue arrow indicates the vector that is normal to the Na–O–Na plane (formed by the central O in the water molecules and the two nearest framework cations).

The blue dashed line represents the projection of the dipole moment on this plane. Theta (in red) is defined as the angle between the dipole and its projection on the Na–O–O plane. Phi (in yellow) is defined as the angle between the projection and the initial projection (yellow dashed line). The green arrow refers is defined based on the positions of the two H atoms in the water molecule. Beta (in green) is defined as the angle between this H–H direction and its initial self (green dashed line).

The distribution $p(\theta, \phi, \beta)$ of these angles then allows one to express the configurational rotational entropy of a water molecule based on the Boltzmann equation [124,125]:

$$S_{\mathrm{rot}} = -k_B\left(\int_0^{\pi} sin\theta d\theta \int_0^{2\pi} d\phi \cdot p(\theta,\phi)\, log\big(p(\theta,\phi)\big) + \int_0^{\pi} d\beta\, p(\beta)\, log\big(p(\beta)\big)\right)$$

Equation 11

where k_{B} is the Boltzmann constant. Here, this integral is discretized to enable their calculation based on the analysis of the MD trajectories. To do this, we cut the angular space of each angle into 1000 bins of the same size and collect the time of appearance of MD-simulated angles in these bins. After normalization, the probability distribution function of each angle can then be numerically approximated, and their integrals along the entire angular space can be calculated through summing all the bins. The reason for separating β from the other two angles is that we assume the librational motion of water molecules is uncorrelated with the change of orientation

of their dipole moments and doing so can greatly decrease computational cost barely losing any accuracy.

The computation of the rotational entropy requires an extended simulation—so that the molecules have enough time to explore their local energy landscape (which is key to enable an accurate computation of the previous integrals). Since such long dynamics is out of reach for *ab initio* MD simulations, we switch to classical MD simulations— which, thanks to their lower computational cost, enable more extended simulations at the cost of some accuracy. Starting from the zeolite structures relaxed by *ab initio* MD, we first conduct a 500 ps relaxation under zero pressure in the *NPT* ensemble—which is long enough to observe a convergence in both volume and energy. For statistical averaging purposes, we then conduct a 1 ns run in the *NVT* ensemble. This duration is long enough to yield a convergence in the computed rotational entropy and enable us to obtain the mean and uncertainty values in a similar way to what we do for heat capacities.

3.2.1.4 Heat capacity

For the calculation of heat capacity, similar to our method of computing entropy, we will combine *ab initio* and classical simulations for the Phonopy simulation itself does not offer accurate results when it comes to hydrated zeolites (Figure 3.2-4 in the results section). However, to maximize the accuracy of *ab initio* simulation, we still only apply the classical simulation to zeolitic water molecules. To do this, we compute the heat capacity of hydrated

zeolites at 300 K, and then only remove the molecules to obtain their dehydrated forms but with the same shapes and volumes and calculate the heat capacity again, so that the difference between the two forms can be understand as the sole contribution from the motion of water molecules. At last, we add this difference to the corresponding results calculated by Phonopy, that is the heat capacity of the dehydrated form of hydrated zeolites with the same shapes and volumes.

To calculate the heat capacity under 300 K for various zeolites, we assume that within a small range near this temperature, Cp, which is the isobaric heat capacity, is a constant. And by calculating the converged average total energy of a zeolite system at a group of temperatures near 300 K, we are able to use linear regression to calculate Cp, which is the slope of the linear relationship. We use the reactive Reaxff force field and choose a time step of 0.5 fs. Starting from the previously NPT-relaxed configuration used in rotational entropy calculation, we conduct five 1-ns run with zero pressure in the NPT ensemble, which are under 280, 290… 320 K. The reason for choosing this 40-K window near 300 K is that we observe ideal linear relationship resemblance of total energies within this range for all eight zeolites that we simulate. And the 10-K difference between each step is to balance the required computational effort and accuracy. Similar for the dehydrated configurations with the same shapes and volumes, we calculate their converged total energies at the same five temperatures but under NVT ensemble to ensure constant volumes and shapes through the MD simulation. The uncertainty values are

obtained by using the same way as entropies, where we add up the uncertainties from the *ab initio* and classical simulations.

3.2.1.5 Dealing with partial occupancies

Finally, it is much more common that any crystal being imperfect rather than perfect. That is, it is usually necessary to define a crystal formula as off-stoichiometric because of the partial atomic occupancies in the crystal lattice. It is an important step that we must go through if we would want our methodology to be further expanded to more common and realistic zeolite situations.

Here, we specifically focus on defected off-stoichiometric zeolites, which is observed in many natural zeolites. In such systems, the average number of certain types of atoms in the unit cell is not an integer, due to reasons such as partial lattice site occupancies or defect [126,127]. However, since molecular dynamic simulations can only model systems comprising of a fixed atomic configuration at the same time, the numbers of atoms must be integers.

Several methods have been introduced to address this difficulty [108,128]. One solution is to enlarge the simulation cell to dimensions that are large enough that partial occupancies can be represented by an integer number of atoms. For example, let us consider the case of mordenite, which has the following unit cell composition: $Ca_{0.289}Na_{0.361}Al_{0.940}Si_{5.060}O_{12}\cdot 3.468H_2O$. Based on this composition, one would need to replicate 1,000 times the unit cell to obtain integer number of atoms, namely: $Ca_{289}Na_{361}Al_{940}Si_{5060}O_{12000}\cdot 3468H_2O$. Clearly, considering such a large system is not practical for *ab initio* simulations, which are typically limited to a few hundreds of atoms. Here,

to address this issue, we propose to describe off-stoichiometric zeolites as a linear combination of stoichiometric zeolites.

We first focus on dehydrated mordenite ($Ca_{0.289}Na_{0.361}Al_{0.940}Si_{5.060}O_{12}$) to illustrate our method. Its configuration is shown in Figure 3.2-2 **a.** All the cations exhibit some partial occupancies on all their possible residing sites according to the IZA databases [115]. Rather than building all the possible unit lattice configurations based on existing atomic site occupancies, we consider a selection of possible unit cell configurations (with integer number of atoms) that can describe the real composition of dehydrated mordenite upon linear combination.

We first focus on the case of Al cations. We first observe that the position of the Al atoms does not influence the thermodynamic properties of the zeolites simulated herein. Note that some network modifiers (in this case, Ca^{2+} and Na^{+}) are needed to charge-compensate the negatively-charged AlO_4 units forming upon the replacement of a Si atom by Al in the network. As such, the numbers of Al atoms and network modifiers in the network are correlated to each other (i.e., to ensure electroneutrality). Therefore, here, the total number of Al is determined after fixing the number of calcium and sodium.

We now focus on the network modifiers (i.e., Ca and Na atoms). In this case, at least three independent configurations (with varying Ca/Si, Na/Si, and Al/Si molar ratios) are needed to account for all the possible stoichiometries by linear combination. The configurations selected herein are shown in Figure 3.2-2 and their compositions are given in ***Table 6***. These compositions are selected so as to be as close as possible to the target composition of dehydrated mordenite. These three models are constructed based on the IZA database [115]. We observe that the divalent

Ca^{2+} cations tend to occupy the center site within rings, while monovalent Na^{+} can be located at both the center and side sites. The thermodynamic properties of these models are then computed based on the methodology developed earlier.

At the exception of the entropy, we assume that the thermodynamic property A_{target} of the target composition can be expressed as a linear combination of those of the stoichiometric models i:

$$A_{\text{target}} = \sum_{i=1}^{3} p_i A_i$$

Equation 12

where A_i is the value the thermodynamic property A for system i and the coefficient p_i is the weights of each model, that is, so that the target composition can be described as a weighted average of the composition of the stoichiometric models i. These weights p_i can easily be determined from a system of linear equations by balancing the amounts of cations of the target (off-stoichiometric) and the simplified models (stoichiometric). In this case, the compositional weights associated with models 1, 2, and 3 are 30%, 45.6%, and 24.4%, respectively.

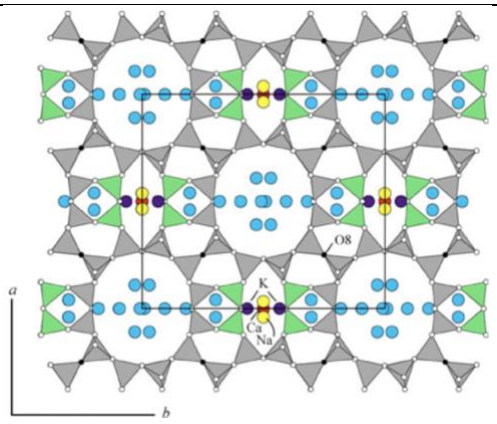

(a)

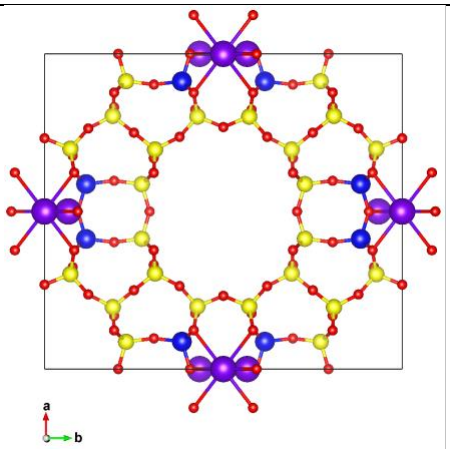

(b)

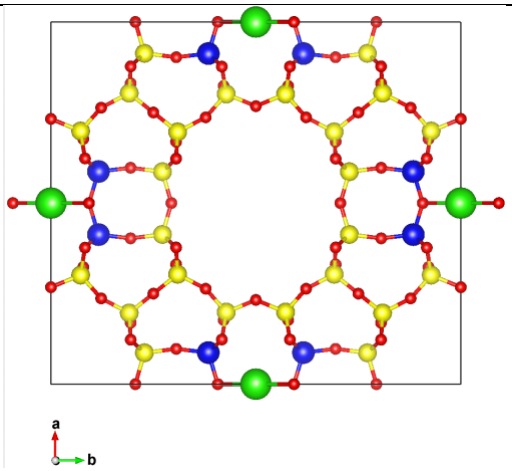

(c)

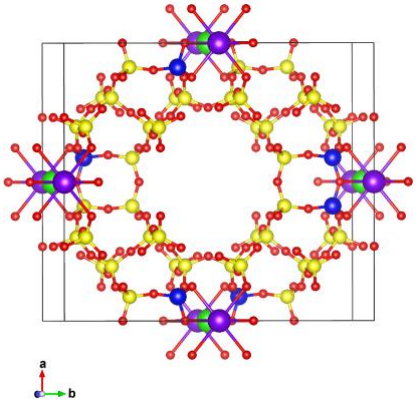

(d)

Figure 3.2-2

(a) Lattice configuration of mordenite-dehydrated [115] and atomic snapshots of the simulation cells of **(b)** model 1 ($NaAlSi_5O_{12}$), **(c)** model 2 ($Ca_{0.5}AlSi_5O_{12}$), and **(d)** model 3

($Ca_{0.25}Na_{0.25}Al_{0.75}Si_{5.25}O_{12}$). Si, Al, Ca, Na, and O atoms are denoted in yellow, blue, green, purple and red, respectively.

In the case of the entropy, we further add (in addition to Equation 12) a combinatorial term capturing the configurational mixing entropy associated with the combination of the three model systems. The mixing entropy is obtained with the following equation [124]:

$$S_{\mathrm{mix}} = \sum_{i=1}^{3} -R p_i \ln(p_i)$$

Equation 13

where R is the ideal gas constant. In the case of mordenite-dehydrated, the mixing entropy is computed as being 8.84 $J \cdot K^{-1} \cdot mol^{-1}$.

In the case of hydrated zeolites, we treat the zeolitic water as follows. Based on each of the three dehydrated models, we build two hydrated models that can be combined so as to give the desired hydrated level by linear interpolation. Using hydrated mordenite (with a composition of $Ca_{0.289}Na_{0.361}Al_{0.940}Si_{5.060}O_{12} \cdot 3.468H_2O$) as an example, reaching an average 3.468 H_2O molecules per unit cell requires us to consider two groups of hydrated configurations each comprising of 3 and 4 water molecules, respectively. This results in a total of six preliminary configurations based on the water positions obtained from the IZA database. To test the influence of different water positions, we vary the H_2O positions in these cells and do all the simulations under the same other conditions. We find that, at constant amount of water, the position of the water molecules in the

network only has a negligible effect on the computed thermodynamic properties—so that we pick the preliminary structure. We then multiply each fraction p_i by 53.2% and 46.8% (i.e., the fractions associated with 3 and 4 water molecules so as to describe the target composition, i.e., 3.468 water molecules per unit cell).

Beside mordenite, we also apply our method to the case of Ca-heulandite ($Ca_{1.07}Al_{2.14}Si_{6.86}O_{18}\cdot 6.17H_2O$). This system is decomposed into four stoichiometric models (see Table 5) associated with the following weights: 81%, 13%, 5%, and 1%, respectively.

Finally, as a final refinement of our method, we find that, rather than directly relaxing zeolites systems under the *NPT* ensemble, conduction an ionic relaxation (VASP code IBRION=2) followed by *NPT* relaxation can dramatically reduce the total relaxation time and, eventually, yield a similar level of convergence in the total potential energy.

3.2.2 Results

The computed values of molar volume, density, formation enthalpy, entropy, and isobaric heat capacity obtained using our methodology for various dehydrated and hydrated zeolites are presented in **Table 1-to-5**, where they are also compared with available experimental and estimated data from various sources. To offer a better visualization of the comparisons, we compare in Figure 3.2-3 to 7 the simulated data with their experimental (or estimated) counterparts.

Table 6-to-10 and Figure 3.2-8 and 9 shows the best results we can get now for off-stoichiometric zeolites. Finally, we will discuss a bit more on the interesting observations on zeolitic water and its effect on volume-based thermodynamics.

3.2.2.1 Molar volume and density

Table 1 **shows** the molar volume and density comparison between our simulated data and experimental values. Besides the 2% errors which indicates good accuracy, notably, we find that, in the case of the dehydrated zeolite, as long as the frameworks are the same, simulated thermodynamic properties only weakly depend on the detail of the zeolite composition and structure. This echoes with previous findings suggesting that zeolites with similar molar volumes (which often arises from the fact that such zeolites have similar frameworks) tend to exhibit highly similar thermodynamic properties. In contrast, the molar volume of hydrated zeolites is more significantly affected by the degree of hydration and, hence, show a greater variability in their thermodynamic properties. In fact, for hydrated zeolites associated with the same framework, the difference in thermodynamic properties resulting from different amount of water per unit cell is much more pronounced than that from different framework compositions.

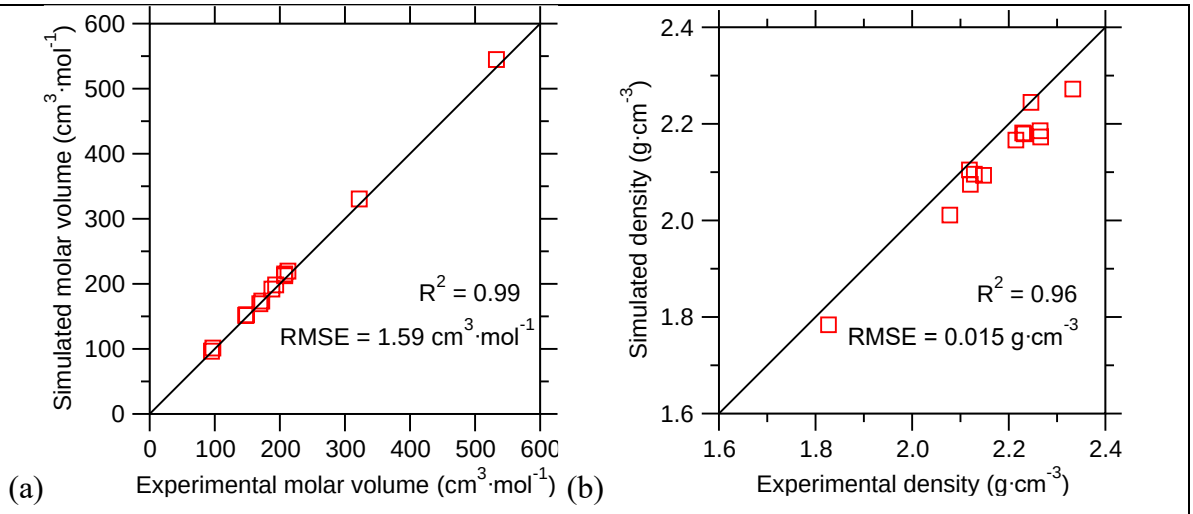

Figure 3.2-3

Simulated **(a)** molar volume and **(b)** density values of the selected zeolite phases at 300 K compared with experimental values. The $y = x$ straight line indicates the locations corresponding to a perfect match between simulations and experiments. Error bars are smaller than the size of the symbols and thus not shown.

Table 1: Computed and reference [102,103] molar volume and density values of the selected zeolites at 300 K .

Zeolites	Formula	Simulated V_m ($cm^3 \cdot mol^{-1}$)	Experimental V_m ($cm^3 \cdot mol^{-1}$)	Simulated Density ($g \cdot cm^{-3}$)	Experimental Density ($g \cdot cm^{-3}$)
Analcime-dehydrated	$NaAlSi_2O_3$	94.9±0.07	96.39 [97]	2.1±0.01	2.10
Natrolite-dehydrated	$Na_2Al_2Si_3O_{10}$	147.5±0.09	151.40 [129]	2.33±0.01	2.27
Wairakite-dehydrated	$CaAl_2Si_4O_{12}$	187.71±0.12	191.84 [130]	2.12±0.01	2.07
Analcime	$NaAlSi_2O_3 \cdot H_2O$	97.09±1.08	101.25 [97]	2.27±0.07	2.17
K-Phillipsite	$KAlSi_3O_8 \cdot 3H_2O$	148.97±3.08	152.21 [102]	2.23±0.05	2.18
Laumontite	$CaAl_2Si_4O_{12} \cdot 4H_2O$	207.53±5.36	215.05 [101]	2.26±0.03	2.19
Natrolite	$Na_2Al_2Si_3O_{10} \cdot 2H_2O$	169.20±0.93	169.31 [100]	2.25±0.01	2.24
Scolecite	$CaAl_2Si_3O_{10} \cdot 3H_2O$	172.30±2.71	173.44 [100]	2.12±0.02	2.10
Wairakite	$CaAl_2Si_4O_{12} \cdot 2H_2O$	193.56±1.32	198.23 [101]	2.23±0.01	2.18
Yugawaralite	$CaAl_2Si_6O_{16} \cdot 4H_2O$	532.83±10.17	544.68 [101]	2.21±0.02	2.17

3.2.2.2 Formation enthalpy

Table 2 shows the simulated formation enthalpies of zeolites and some of their dehydrated counterparts, and all data are compared either with experimental or theoretically estimated values. Generally, the simulated data present an ideal match with reference data–with relative errors below 2%. These demonstrate the power of ab initio simulation in computing the enthalpy of formation for simple zeolites, and thus pave way for our future efforts towards simulating more complex configurations (e.g. zeolites with partial occupancies and defects).

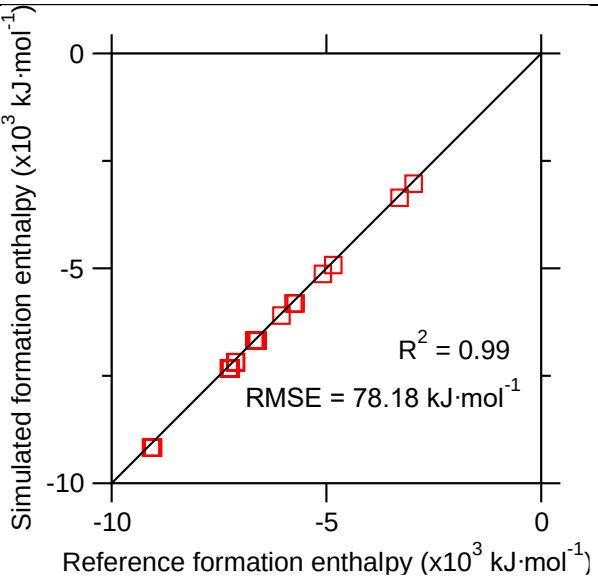

Figure 3.2-4

Simulated formation enthalpy values of zeolites compared with experimental and estimated (red squares) values. The $y = x$ straight lines indicate the locations corresponding to a perfect

match between simulations and experiments. Error bars are smaller than the size of the symbols and thus not shown.

Table 2: Simulated formation enthalpy of some zeolites at 300 K. Data are compared with experimental and estimated results.

Zeolites	**Formula**	**Simulated $\Delta_f H$ (kJ·mol^{-1})**	**Experimental $\Delta_f H$ (kJ·mol^{-1})**	**Estimated $\Delta_f H$ (kJ·mol^{-1})**	**Relative difference (%)**
Analcime-dehydrated	$NaAlSi_2O_3$	-3031.80±16	-2970.2±3.5 [97]		2.07
Metaleonhardite	$CaAl_2Si_4O_{12}$	-6043.30±37	-5964.30 [101]		1.32
Natrolite-dehydrated	$Na_2Al_2Si_3O_{10}$	-5130.30±32	-5082.90 [102]		0.93
Analcime	$NaAlSi_2O_3 \cdot H_2O$	-3360.00±25	-3296.9±3.3 [97]		1.91
Laumontite	$CaAl_2Si_4O_{12} \cdot 4H_2O$	-7332±54	-7251.0±8.5 [101]		1.12
			-7268.90±6.3 [101]		0.87
			-7231.3±10.1 [101]		1.39
			-7233.6 [101]		1.36

Leonhardite	$CaAl_2Si_4O_{12}\cdot 3.5H_2O$	-7185.80±39	-7107.3±5.6 [101]		1.10
			-7123.2±4.8 [101]		0.88
			-7108.3±5.2 [101]		1.09
K-Phillipsite	$KAlSi_3O_8\cdot 3H_2O$	-4923.85±41		-4841.86 [102]	1.69
Natrolite	$Na_2Al_2Si_3O_{10}\cdot 2H_2O$	-5818.50±32	-5769.9±5.0 [100]		0.84
				-5718.60 [102]	1.75
Scolecite	$CaAl_2Si_3O_{10}\cdot 3H_2O$	-6099.17±30	-6049.0±5.0 [100]		0.83
Wairakite	$CaAl_2Si_4O_{12}\cdot 2H_2O$	-6680.64±34	-6646.7±6.3 [101]		0.51
			-6678.9±5.0 [101]		0.03
			-6606.90±8.1 [101]		1.12
			-6608.80 [101]		1.09
Yugawaralite	$CaAl_2Si_6O_{16}\cdot 4H_2O$	-9172.28±78	-9051.30±10.4 [101]		1.34
			-9036.19 [101]		1.51
				-9087.60 [106]	0.93

3.2.2.3 Entropy

Though Phonopy itself yields accurate entropy predictions for dehydrated zeolites, on the other hand, the entropy and heat capacities predicted by Phonopy for hydrated zeolites are systematically underestimated as compared to experimental data (Figure 3.2-5) and the accuracy is thus not as satisfying as the simulated results of formation enthalpy. This can be understood from the fact that Phonopy yields the entropy contribution arising from phonon vibration, which is the main contribution to the total entropy in non-hydrated zeolites. However, hydrated systems exhibit non-negligible additional degrees of freedom, namely, the rotational and translational motions modes of water molecules. The contribution of these degrees of freedom to the total entropy is not captured by the Phonopy calculation. This urges us to develop a corrective method that can explicitly calculate the rotational entropy of zeolitic water molecules that can make up to the Phonopy results.

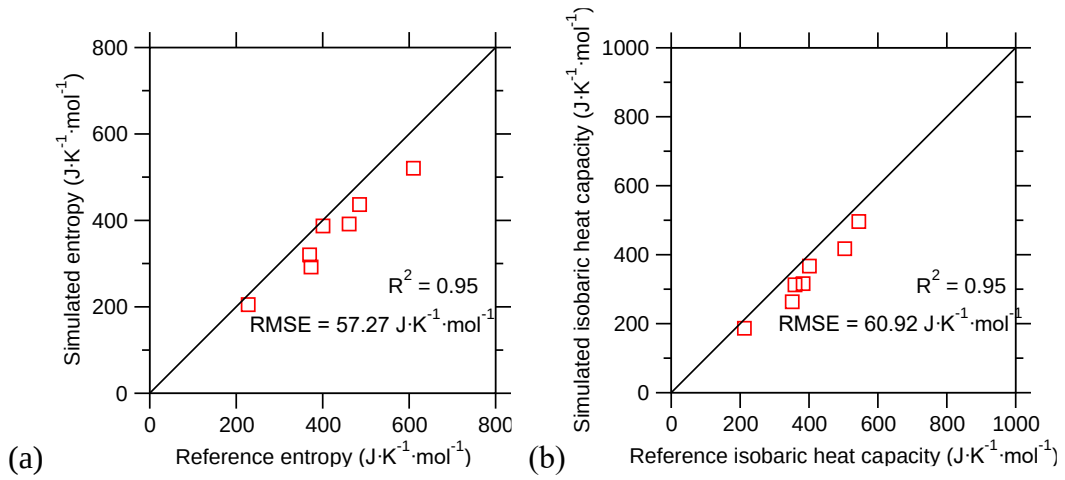

Figure 3.2-5

Phonopy-calculated **(a)** entropy and **(b)** heat capacity values of the selected zeolite phases at 300 K compared with experimental values. The $y = x$ straight line indicates the locations corresponding to a perfect match between simulations and experiments. Error bars are smaller than the size of the symbols and thus not shown.

Table 3 shows components of simulated rotational entropy (Theta and phi refers to the dipole orientation of the water molecules, and beta describes their librational motions) the while ***Table 4*** combines the vibrational entropy, rotational entropy associated with water molecules, and total entropy values for all simulated zeolites compared to experimental data. Overall, we observe that the computed entropy values (i.e., comprising both the vibrational and rotational terms) exhibit a very good agreement with experimental data. We also find from that the librational motion

contributes the most to increasing the rational entropy of the water molecules. Nevertheless, we find that the computed librational entropy values are systematically lower than 24.5 $J \cdot K^{-1} \cdot mol^{-1}$ (which is the ideal entropy associated with a free, unconstrained librational rotator). This highlights the important role played by the zeolite structure in constraining the rotational motion of the water molecules that are present in their structures.

Figure 3.2-7 compares the angular distributions of two signature water molecules from Analcime and Laumontite: the water molecule in analcime where all the water is topologically the same, and the type 3 water in laumontite which we refer to the channel water that sits in the middle of the 10-membered rings. We observe that analcime exhibits notably sharper distributions, for each of the three angles. This indicates that the water molecules in laumontite features a significant rotational mobility, whereas, in contrast, the orientation of the water molecules is more constrained in analcime. This echoes the fact that the water molecules are more confined in analcime. This offers a good example of the vastly different behaviors of zeolitic water in various situations and thus proves that it is not wise to apply any universal correction to the entropy of zeolitic water molecules.

Table 3: Simulated phi, theta and beta angular entropy data and their sum for various zeolites (water molecules in the same zeolite but of different topological type are listed separately).

Zeolites	Theta and Phi entropy $J \cdot K^{-1} \cdot mol^{-1}$	Beta entropy $J \cdot K^{-1} \cdot mol^{-1}$	Rotational entropy $J \cdot K^{-1} \cdot mol^{-1}$
Analcime	0.52±0.09	13.08±0.99	13.60±1.08
Wairakite	7.68±0.89	14.50±2.28	22.18±3.17
Laumontite water 1	4.12±0.32	12.50±3.74	16.62±4.06
Laumontite water 2	9.55±0.87	14.24±3.51	23.79±4.38
Laumontite water 3	9.53±1.08	13.95±3.39	24.48±4.47
Leonhardite water 1	4.54±0.28	12.59±3.04	17.13±3.32
Leonhardite water 2	9.03±0.62	14.85±3.27	23.88±3.89
Natrolite	1.05±0.23	13.37±1.41	14.50±1.64
Scolecite	4.85±0.32	14.48±1.70	19.65±2.02
Yugawaralite	5.86±0.39	12.92±2.05	18.78±2.44
K-Phillipsite	4.83±0.32	14.38±3.21	19.21±3.53

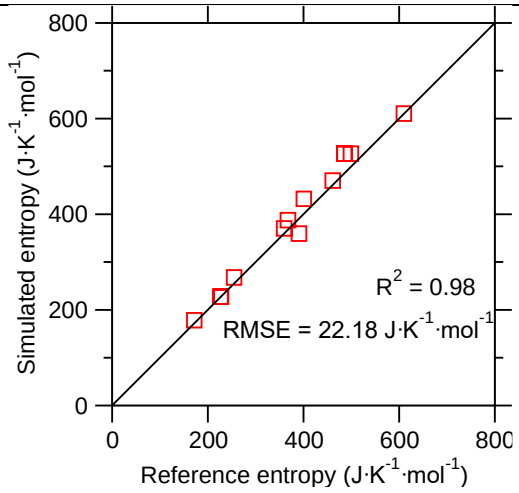

Figure 3.2-6

Computed entropy values of the selected zeolite at 300 K compared with experimental (red square) and estimated (blue diamond) values. The y = x straight line indicates the locations corresponding to a perfect match between simulations and experiments. Error bars are smaller than the size of the symbols and thus not shown.

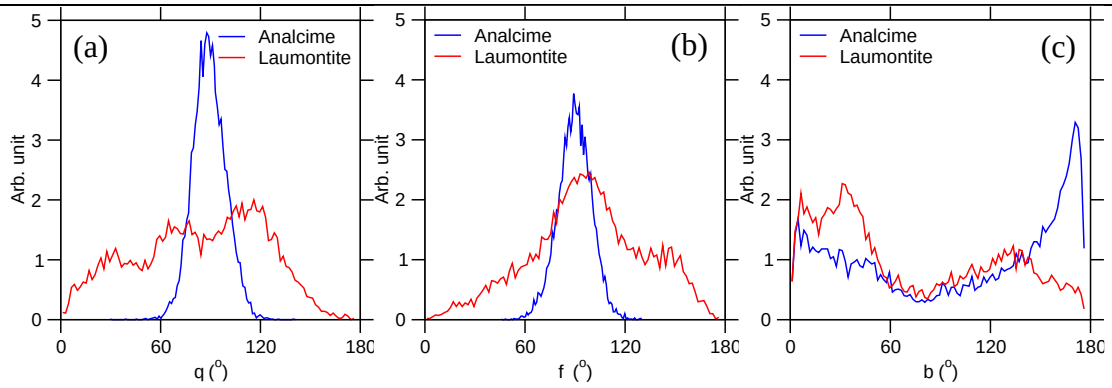

Figure 3.2-7

Angular distributions of the (a) theta, (b) phi, and (c) beta angles defining the orientation of water molecules in analcime and laumontite. Here, though beta angles for both zeolites have a wide distribution (indicating a free libration movement), the theta and phi angles of waters in analcime have much sharper distributions than those in laumontite (the dipole orientation is much more constrained for water in analcime than in laumontite).

Table 4: Simulated values of the vibrational (computed by Phonopy) and rotational (computed based on classical MD) entropy for all the zeolitic phases considered herein. Experimental values are indicated for comparison. Numbers in the parenthesis indicates the number of water molecules in the formula unit.

Zeolites	**Formula**	**Vibrational entropy ($J \cdot K^{-1} \cdot mol^{-1}$)**	**Rotational entropy ($J \cdot K^{-1} \cdot mol^{-1}$)**	**Total simulated entropy ($J \cdot K^{-1} \cdot mol^{-1}$)**	**Experimental or estimated entropy ($J \cdot K^{-1} \cdot mol^{-1}$)**	**Relative difference (%)**
Analcime-dehydrated	$NaAlSi_2O_3$	178.32±0.37	-	178.32±0.37	171.71±0.17	3.85
Metaleonhardite	$CaAl_2Si_4O_{12}$	267.70±0.51	-	267.70±0.51	255.00	4.98
Analcime (1)	$NaAlSi_2O_3 \cdot H_2O$	205.63±10.62	13.60±1.08	219.23±12	226.75±0.23 [131]	3.32
Wairakite (2)	$CaAl_2Si_4O_{12} \cdot 2H_2O$	387.01±14.33	22.18±3.17	431.37±18	400.70 [101]	7.65
Laumontite (3)	$CaAl_2Si_4O_{12} \cdot 4H_2O$	436.66±18.79	16.62±4.09	504.70±23	485.30±20.9 [101]	4.00
Leonhardite (3)	$CaAl_2Si_4O_{12} \cdot 3.5H_2O$	391.69±17.31	17.13±3.32	460.92±21	461.10±5.45 [101]	0.04
Natrolite (2)	$Na_2Al_2Si_3O_{10} \cdot 2H_2O$	325.42±12.50	14.50±1.64	348.42±14	359.73±0.72 [100]	3.14

Scolecite (3)	$CaAl_2Si_3O_{10}·3H_2O$	320.11±15.17	19.65±2.02	367.06±17	367.42±0.73 [100]	1.00
Yugawaralite (4)	$CaAl_2Si_6O_{16}·4H_2O$	520.99±12.87	18.78±2.44	596.11±15	609.80 [101]	2.24
K-Phillipsite (3)	$KAlSi_3O_8·3H_2O$	337.27±14.19	19.21±3.53	394.90±18	390.57 [103]	1.11

3.2.2.4 Heat capacity

Table 5 exhibits the heat capacities of dehydrated zeolites, the dehydrated forms of hydrated zeolites with removed water molecules, and their corresponding hydrated zeolites. All data are compared to experimental data. We can see that the errors are generally within 5%, which indicates a good matching of our data to experiments. Moreover, we find that this method that combines *ab initio* and classical MD yields a higher accuracy than using Phonopy calculation alone (comparison shown supplementary materials). This emphasizes the fact that classical simulation is necessary in completely describing the motions of zeolitic water molecules and giving more accurate thermodynamic computation results, while only considering vibrational effects is insufficient when it comes to various hydrated zeolites with different environments for framework water molecules.

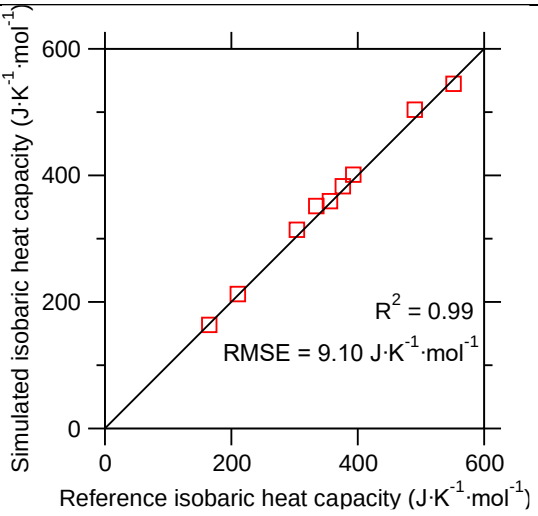

Figure 3.2-8

Computed isobaric heat capacity values of the selected zeolite at 300 K compared with experimental (red square) values. The $y = x$ straight line indicates the locations corresponding to a perfect match between simulations and experiments. Error bars are smaller than the size of the symbols and thus not shown.

Table 5: Simulated values of the isobaric heat capacity for all the zeolitic phases considered herein. Numbers in the parenthesis indicates the number of water molecules in the formula unit.

Zeolites	**Formula**	**Simulated C_p ($J \cdot K^{-1} \cdot mol^{-1}$)**	**Experimental C_p ($J \cdot K^{-1} \cdot mol^{-1}$)**	**Relative difference (%)**
Analcime-dehydrated	$NaAlSi_2O_3$	165.06±0.28	163.59±0.16 [131]	0.903

Metaleonhardite	$CaAl_2Si_4O_{12}$	303.74±1.97	314.04 [101]	3.39
Analcime (1)	$NaAlSi_2O_3 \cdot H_2O$	210.27±7.54	212.38±0.21 [131]	0.995
Wairakite (2)	$CaAl_2Si_4O_{12} \cdot 2H_2O$	392.88±8.72	401.04 [101]	2.03
Laumontite (3)	$CaAl_2Si_4O_{12} \cdot 4H_2O$	490.32±13.98	503.71 [101]	2.66
Natrolite (2)	$Na_2Al_2Si_3O_{10} \cdot 2H_2O$	356.03±14.35	359.23±0.72 [100]	0.891
Scolecite (3)	$CaAl_2Si_3O_{10} \cdot 3H_2O$	376.42±11.60	382.81±0.73 [100]	1.67
Yugawaralite (4)	$CaAl_2Si_6O_{16} \cdot 4H_2O$	551.60±9.25	544.68 [101]	-1.27
K-Phillipsite (3)	$KAlSi_3O_8 \cdot 3H_2O$	334.43±7.87	351.41 [103]	4.83

3.2.2.5 Off-stoichiometric zeolites

The calculated properties obtained using the linear combination method for dehydrated and hydrated mordenite are presented in ***Table 6***,

Table *7* and Figure 3.2-9, wherein they are compared with experimental values. Further, the thermodynamic properties of the six stoichiometric models constructed herein to describe dehydrated and hydrated mordenite is compared with estimated values from Zhen-Wu *et al* [132],

Table 8—since no experimental data are available for these models. Calculated properties obtained from the simulated Ca-heulandite models are compared to experiments in ***Table 9*** and with estimated values ***Table 10***, as well as Figure 3.2-10.

Overall, we find that the simulated formation enthalpies agree very well with experimental values, with relative errors that are below 1%. The simulated entropy values also exhibit a good agreement with experimental data, which highlight the need to carefully account for the mixing entropy correction. Notably, we find that, in the case of the dehydrated zeolite models, as long as the frameworks are the same, simulated thermodynamic properties only weakly depend on the detail of the zeolite composition and structure. This echoes with previous findings suggesting that zeolites with similar molar volumes (which often arises from the fact that such zeolites have similar frameworks) tend to exhibit very similar thermodynamic properties [103,132]. In contrast, the molar volume of hydrated zeolites is more significantly affected by the degree of hydration and, hence, show a greater variability in their thermodynamic properties. This is clearly shown in Figure 3.2-9 **(b)** and Figure 3.2-10 **(b)**, where the difference in formation enthalpies resulting from different amount of water per unit cell is much more pronounced than that from different cation compositions. Finally, the overall harmony between simulated, estimated, and experimental values strongly supports the capability of the linear combination method introduced herein to yield accurate predictions of the thermodynamic properties of zeolites with partial atomic site occupancies, which may otherwise be difficult to simulate using conventional methodologies.

Table 6: Simulated thermodynamic data of dehydrated mordenite at 300 K, as obtained for all the simple stoichiometric models, as well as the target composition. Data are compared with available experimental data.

Zeolites	Formation enthalpy $\Delta_f H$ (kJ·mol^{-1})	Entropy S (J·K^{-1}·mol^{-1})	Isobaric heat capacity C_p (J·K^{-1}·mol^{-1})
$NaAlSi_5O_{12}$ (Model 1)	-5684.38	290.50	276.68
$Ca_{0.5}AlSi_5O_{12}$ (Model 2)	-5666.45	285.59	278.44
$Ca_{0.25}Na_{0.25}Al_{0.75}Si_{5.25}O_{12}$ (Model 3)	-5671.64	281.65	275.07
$Ca_{0.289}Na_{0.361}Al_{0.940}Si_{5.060}O_{12}$ (Target)	-5675.89	294.94	277.09
Mordenite dehydrated	-5661.8±4.60 [133]	299.10±0.60 [133]	295.76±0.59 [103]

Table 7: Simulated thermodynamic data of hydrated mordenite at 300 K, as obtained for all the simple stoichiometric models, as well as the target composition. Data are compared with available experimental data.

Zeolites	Formation enthalpy $\Delta_f H$ (kJ·mol^{-1})	Entropy S (J·K^{-1}·mol^{-1})	Isobaric heat capacity C_p (J·K^{-1}·mol^{-1})
$NaAlSi_5O_{12}\cdot 3H_2O$ (Model 1)	-6679.23	498.6076	416.715
$NaAlSi_5O_{12}\cdot 4H_2O$ (Model 2)	-6870.33	530.97	465.37
$Ca_{0.5}AlSi_5O_{12}\cdot 3H_2O$ (Model 3)	-6745.41	477.0195	406.5146
$Ca_{0.5}AlSi_5O_{12}\cdot 4H_2O$ (Model 4)	-6990.54	510.6691	460.178
$Ca_{0.25}Na_{0.25}Al_{0.75}Si_{5.25}O_{12}\cdot 3H_2O$ (Model 5)	-6648.24	470.376	407.896
$Ca_{0.25}Na_{0.25}Al_{0.75}Si_{5.25}O_{12}\cdot 4H_2O$ (Model 6)	-6808.95	512.43	459.34
$Ca_{0.289}Na_{0.361}Al_{0.940}Si_{5.060}O_{12}\cdot 3.468H_2O$ (Target)	-6799.32	501.675766	435.295267
Mordenite hydrated	-6738.44 [133]	486.54 [133]	484.33 [103]

Table 8: Simulated thermodynamic data of the dehydrated and hydrated mordenite stoichiometric models at 300 K. Data are compared with estimated results.

Zeolites	Simulated $\Delta_f H$ (kJ·mol^{-1})	Estimated $\Delta_f H$ (kJ·mol^{-1})	Simulated S (J·K^{-1}·mol^{-1})	Estimated S (J·K^{-1}·mol^{-1})	Simulated C_p (J·K^{-1}·mol^{-1})	Estimated C_p (J·K^{-1}·mol^{-1})
Model 1	-6679.23	-6597.55	498.6076	501.32	416.715	453.895
Model 2	-6870.33	-6883.39	530.97	532.635	465.37	508.96
Model 3	-6745.41	-6629.42	477.0195	475.55	406.5146	455.12
Model 4	-6990.54	-6915.22	510.6691	506.3925	460.178	500.25
Model 5	-6648.24	-6535.43	470.376	477.9125	407.896	444.7
Model 6	-6808.95	-6821.27	512.43	508.84	459.34	499.8775

Table 9: Simulated thermodynamic data of hydrated Ca-heulandite at 300 K, as obtained for all the simple stoichiometric models, as well as the target composition. Data are compared with available experimental data.

Zeolites	**Formation enthalpy $\Delta_f H$ (kJ·mol^{-1})**	**Entropy S (J·K^{-1}·mol^{-1})**	**Isobaric heat capacity C_p (J·K^{-1}·mol^{-1})**
$CaAl_2Si_7O_{18}\cdot 6H_2O$ (Model 1)	-10345.55	695.31	695.95
$Ca_{1.5}Al_3Si_6O_{18}\cdot 6H_2O$ (Model 2)	-10530.56	703.11	702.37
$CaAl_2Si_7O_{18}\cdot 9H_2O$ (Model 3)	-11490.00	858.95	850.61
$Ca_{1.5}Al_3Si_6O_{18}\cdot 9H_2O$ (Model 4)	-11753.20	866.63	861.63
$Ca_{1.07}Al_{2.14}Si_{6.86}O_{18}\cdot 6.17H_2O$ (Target)	-10517.78	718.68	718.00
Ca-heulandite	-10667.2 [106]	700.94 [106]	729.87 [106]

Table 10: Simulated thermodynamic data of the Ca-heulandite stoichiometric models at 300 K. Data are compared with estimated results.

Zeolites	Simulated $\Delta_f H$ (kJ·mol^{-1})	Estimated $\Delta_f H$ (kJ·mol^{-1})	Simulated S (J·K^{-1}·mol^{-1})	Estimated S (J·K^{-1}·mol^{-1})	Simulated C_p (J·K^{-1}·mol^{-1})	Estimated C_p (J·K^{-1}·mol^{-1})
Model 1	-10345.55	-10294.91	695.31	732.46	695.95	734.96
Model 2	-10530.56	-10468.97	703.11	742.64	702.37	736.43
Model 3	-11490.00	-11402.30	858.95	891.41	850.61	895.09
Model 4	-11753.20	-11666.49	866.63	895.56	861.63	900.97

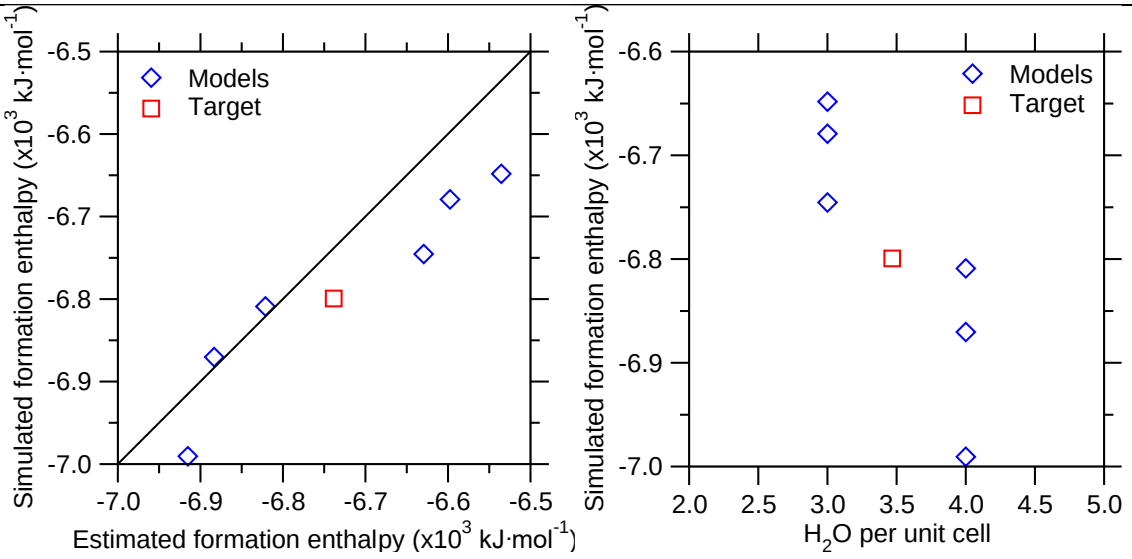

Figure 3.2-9

(a) Formation enthalpy of the mordenite stoichiometric model (blue diamonds) as a function of the estimated values. The red square symbol shows the comparison between the value calculated by linear combination for the target composition and the estimated value. The $y = x$ straight line indicates denotes a perfect match between simulations and estimations. **(b)** Formation enthalpy of the mordenite stoichiometric models (blue diamonds) and of the target composition (obtained by linear combination, red squares) as a function of the number of water molecules per unit cell.

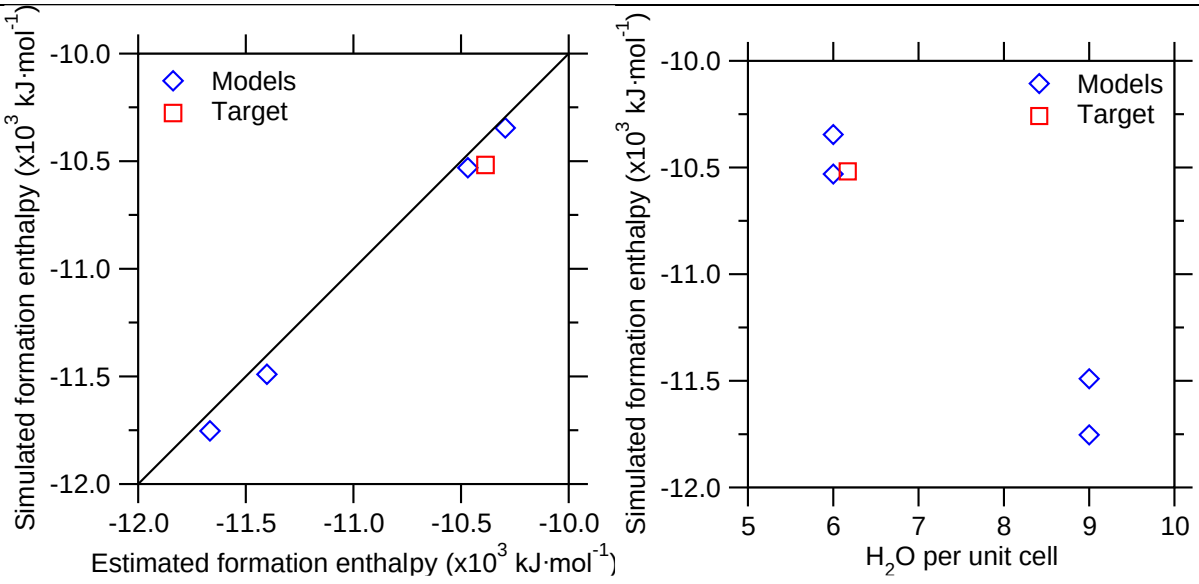

Figure 3.2-10

(a) Formation enthalpy of the Ca-heulandite stoichiometric model (blue diamonds) as a function of the estimated values. The red square symbol shows the comparison between the value calculated by linear combination for the target composition and the estimated value. **(b)** Formation enthalpy of the Ca-heulandite stoichiometric models (blue diamonds) and of the target composition (obtained by linear combination, red squares) as a function of the number of water molecules per unit cell.

3.2.2.6 Other findings

Next, we further explore the nature of the relationship between rotational entropy and the local volume that is accessible to water molecules. Figure 3.2-11 shows the relationship between the rotational entropy per water molecule and the average local volume that is accessible to them. We observe the existence of a logarithmic relationship between rotational entropy and local volume, which echoes the predictions from free volume theory [134–137]. This indicates that the rotational entropy exhibited by water molecules in zeolitic phases depends on their degree of confinement—wherein confined water molecules have accessed to smaller local volume and, hence, tend to exhibit smaller rotational entropy values. As a reference, the volume that is accessible to the water molecules in liquid water under atmospheric condition is 29.90 $Å^3$. Interestingly, we find by extrapolation that the water molecules would exhibit a zero rotational entropy at a local volume of 12.68 $Å^3$. This value echoes the value of 14.6 $Å^3$, which corresponds to the "solid" volume of the atoms a water molecule is made of. This suggests that the entropy of water molecules would vanish if their local volume became roughly equal to the solid volume of the water molecules—which, in this case, would prevent any motion of the water molecules. This supports the idea that the rotational entropy scales with the free volume that is accessible to the water molecules (that is, the difference between the total local volume and the solid volume of the water molecules) [138,139].

Finally, Figure 3.2-12 shows the correlation between local volume and three types of rotational entropy. Overall, we find that the entropy terms associated with the theta and phi angles exhibit

the most pronounced correlation with local volume. This indicates that these models of motion are especially sensitive to the structure of the zeolitic phase. In contrast, the entropy term associated with the beta angle (libration motion) remains fairly affected and only exhibits a minor dependance on the local volume that is accessible to the water molecules. This indicates that the libration motion of the water molecules (i.e., rotation along the directional of their dipole moment) is notably less constrained by the surrounding zeolite structure than the two other modes of rotation.

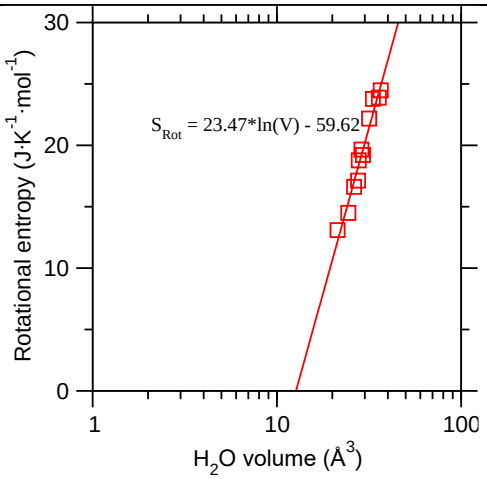

Figure 3.2-11

Rotational entropy per water molecule as a function of the local volume that is accessible to them. The data are fitted by a logarithmic function.

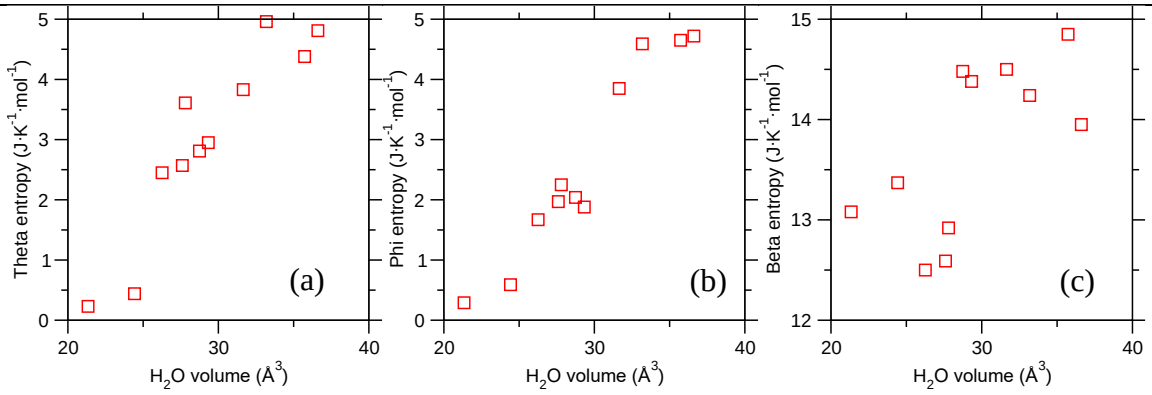

Figure 3.2-12

Three rotational entropy terms associated with the (a) theta, (b) phi, and (c) beta angles orientational angles as a function of the local volume that is accessible to the water molecules.

3.2.3 Conclusions

Altogether, the overall harmony between simulated, estimated, and experimental values strongly supports the capability of our methodology and corrections introduced herein to yield accurate predictions of the thermodynamic properties of zeolites of various structures and compositions. The combination of ab initio and classical molecular dynamics simulation not only has the power to accurately evaluate the properties of zeolite framework atoms, but also completely describe the equilibrium kinetic behaviors of zeolitic water molecules, which give access to even higher

accuracy of computing the entropy and heat capacity of hydrated zeolites than using AIMD alone. This offers a robust methodology to use MD to generate thermodynamic data for zeolite phases that are presently missing from existing databases.

3.3 GEMS modeling of zeolite formation

The object of this part is to use the thermodynamic data we get from step 1 for over 20 types of zeolites to calculate their precipitation maps using the GEM Selektor (GEMS) software. Thanks to the definitive work of Zhen-Wu *et al.* [33,140], we can gain access to the zeo19 GEMS database [140]– a complete collection of zeolite thermodynamic data from experiments that is specifically designed under the GEMS environment. We will use zeo19 as a reference to validate the stability field and precipitation mapping we calculate using our data and show that our results yield high accuracy.

3.3.1 Method

3.3.1.1 Working mechanisms of GEM Selektor

GEMS (Gibbs Energy Minimization Selektor) is a program that is commonly used to model geochemical systems of solid solutions and aqueous complexes by using the principles of local and partial equilibrium [141,142]. The working mechanisms of GEMS can be summarized as the following equation using classical thermodynamic identities:

$$\Delta_r H - T\Delta_r S \equiv \Delta_r G = -RTlnK$$

Equation 14

where $\Delta_r H$, $\Delta_r S$, $\Delta_r G$ are the reaction enthalpy, entropy and Gibbs free energy change for a specific chemical reaction, and K is the solubility constant. That is, in the case of predicting zeolite precipitation in a solution, given the formation enthalpy and entropy of a specific zeolite, we can calculate its solubility constant at any given temperature. Then, given the types and amounts of all reactants (in our case, the composition of the dissolving glass, or the amounts of various oxides including SiO_2, Al_2O_3, B_2O_3, Na_2O, etc.) and pH, we can estimate the amount (in the unit of mass or mole) of zeolite product. Note that, because we are always considering many kinds of zeolites together as potential products instead of one at a time, a chemical equilibrium must be reached before the precipitation simulation, which is provided in the GEMS functions.

3.3.2 Result

We use selected experimental data and the zeo19 database as the reference for the validation of our results, and the validation process is composed of two ways of demonstration of GEMS simulation results: 1) the stability fields and 2) precipitation mapping.

Figure 3.3-1 shows one example of the many stability fields that we have calculated and its comparison to the same situation calculated by Zhen-Wu *et al.* using the zeo19 database [140]. Here, for the simplicity of reading, we use the International Simple Glass (ISG) as the initial composition and the simulation is done at T = 90 ^{o}C, which is a common situation for the nuclear waste immobilization glasses. The first thing we notice is that analcime is the only zeolite we get among all 20 types of zeolites. This is the same with what Zhen-Wu *et al.* discover in their paper where they deem this result reasonable and owe this to the stability of analcime compared to other zeolites. Next, we find that the stability boundaries for all products in terms of pH that we calculate agree well with the results from Zhen-Wu *et al.* This means that the precipitation starting pH we calculate, which is the key output value we will use for machine learning model training in the next part, is accurate and could be used for further data harvesting. Moreover, we find that, at the typical underground temperatures experienced by nuclear glass ranging from 25 to 90 ^{o}C, only the zeolites that form at a pH higher than ~ 10 can be well validated by experimental results. We thus consider those forming at a pH too low to be invalid and remove them from the product pool for a specific situation. The only pronounced difference between our results and theirs appears to be the volume fraction limit between amorphous silica, calcium

alkali aluminosilicate hydrate (C–N–A–S–H) and the rest phases. We believe that this difference mainly comes from the fact that they consider a much simpler pool of fewer types of zeolites and other possible products, which they do not mention in details, where the competitive effect among products is weaker. Finally, by comparing a and b, we can see that a higher solid to liquid ratio will lengthen the precipitation area of zeolites towards higher pH, which is the consequence of reaching different chemical equilibria.

Figure 3.3-2 shows the GEMS-predicted precipitation lower (the earliest of any zeolite formation) and higher (the latest of any zeolite precipitation) pH limit as a function of simulation temperature for all considered zeolites from an ISG dissolution. The two limits therefore depict a region where there are zeolite precipitations. We find that our estimation agrees well with experimental data and correctly shows the trend of the precipitation region grow towards top left with higher temperatures, which can be simply understood as higher temperatures can provide stronger thermo-activation and thus make the formation of zeolites "easier" (at lower pH). Additionally, we find that the lower limit at 90 ^{o}C shown in all the experiments is about pH = 10.7, and higher at lower temperatures. This supports our removal of zeolites that form at low pH under low temperatures.

(a)

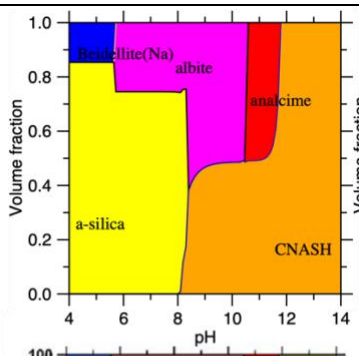

(b)

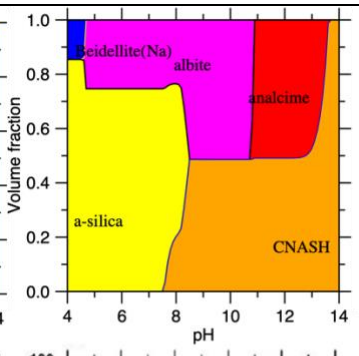

(c)

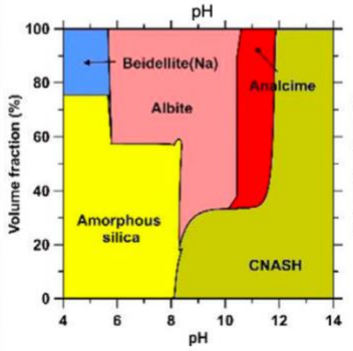

(d)

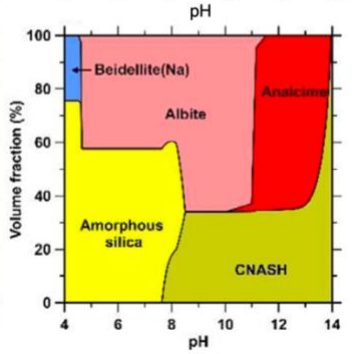

Figure 3.3-1

GEMS-simulated stability fields of ISG dissolution at 90 °C. (a) and (c): solid-to-liquid ratio = 0.1, (b) and (d) S/L = 1. (c) and (d) are results calculated by Zhen-Wu *et al* [140].

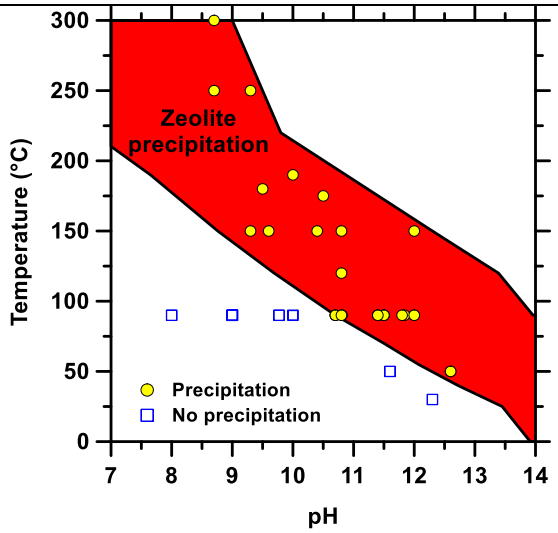

Figure 3.3-2

Precipitation region of zeolites in terms of pH and temperature. Yellow circles and blue squares are data collected from experiments.

3.4 Prediction of zeolite precipitation

In this part, we will finalize the entire chapter by training a machine learning (ML) – based model that can predict the lower limit of zeolite formation pH using the factors considered thus far (glass composition and temperature) as input data. We must point out that, since ML training typically requires tens of thousands of data points (or even more for complex relationships), the result from part is far from being perfect and should continue to be updated with more data

obtained from 3.3. What we are showing here is a preliminary and heuristic methodology that should be considered as a starting point instead of finishing point for future researchers.

3.4.1 Method

As mentioned earlier, we use the glass composition (the amounts of Na_2O, CaO, Al_2O_3, B_2O_3, SiO_2, K_2O and MgO reactants) and temperature as input, and the lower limit of zeolite precipitation pH as output. Note that we will keep the solid to liquid ratio as 0.1 to best simulate the realistic situation (these can also be changed for specific future research interest). We use a total of 3000 GEMS data points where the input is generated randomly for the best learning results. We also set a range for each oxide based on the empirical value of the limit of oxides in glasses, except for SiO_2 for which we treat as a compensating element (its amount is calculated by 100% - the sum of the fractions of the components) to the other oxides and the main building block (it has a higher fraction than any other components) of all the glasses. We apply a neural network (NN) regressor as the base model of our training and testing. Before using NN, we try simpler regression algorithms such as linear, polynomial and random forest but the learning results are all way behind NN, which is the reason why we make this decision.

The network perimeter that we have tuned to give the best result so far can be described as the following:

The network consists of three layers, all followed by a ReLU activation function for backward propagation: 1) 64 neurons, 2) 16 neurons, 3) 4 neurons. We divide the training and test data set as 85% to 15% and continue to exchange the data points in both sets for the most accurate results. The batch size is chosen to be 512 to work with the total data points number of 3000. The learning rate and weigh decay is chosen to be 5e-2 and 1e-6 separately, and we run 1000 epochs to avoid overfitting.

In addition, we apply SHAP to assess the impact of each feature on zeolite precipitation.

3.4.2 Result

The learning result is shown in Figure 3.4-1. A testing root-mean-square error (RMSE) value of 0.6 is currently the best we can achieve with our NN model. This means we now have the power to estimate the precipitation pH lower limit within a range of ± 0.6 centered around the GEMS estimated value. Other perimeter either underfit (training and test RMSE are both high) or overfit (training RMSE is very low but test RMSE higher than underfitting situations) the data points.

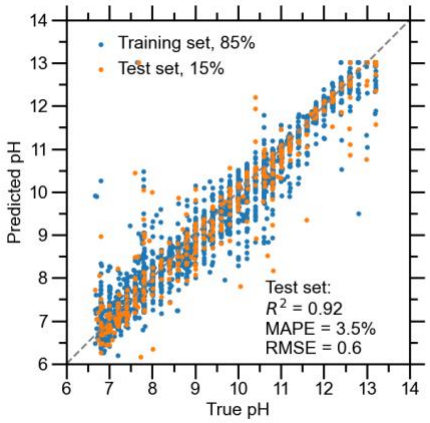

Figure 3.4-1

Comparison between predicted and true pH values from the training set and test set. The dashed diagonal indicates the perfect match.

We can also observe some interesting results from the SHAP data (shown in Figure 3.4-2). We first notice that Na_2O has the greatest impact on zeolite formation among the other oxides. This can be understood through the following reasons: 1) Na is the most common network modifier seen in zeolites and the zeolites pool we consider [97,100–102,140], 2) the Na cation has the strongest affiliation with the aluminosilicate network and in-lattice water molecules [130,143–145], which is also shown in 3.2. This will make the Na cation harder to dissociate from the glass network compared to other cations and can act as a binder of the entire system. This explains why Na_2O is appearing to have positive impact on the zeolite precipitation pH (a higher Na_2O value will increase the pH, that is, making zeolite precipitation harder). Next, the amount of alumina, calcium oxide and temperature all have a negative impact on the pH which means that a higher

value would make zeolite precipitation happen at a lower pH, or, more easily. The impact of alumina can be understood as a mismatch as well as competition with silica, that is, the system structurally prefers to have a complete silica network instead of a mixed one when the glass is mainly comprised of silica [107,145]. Different from sodium oxide, the Ca cation is much larger and usually loosely confined in pores and voids in the glass network [101,106]. This would make its diffusion propensity stronger than its binding effects of the network and thus contribute to the precipitation of secondary phases outside the dissolved glass. Other oxides only rarely appear in any zeolites and their SHAP-calculated impact is so weak that is close to 0 and we hide them from the plot.

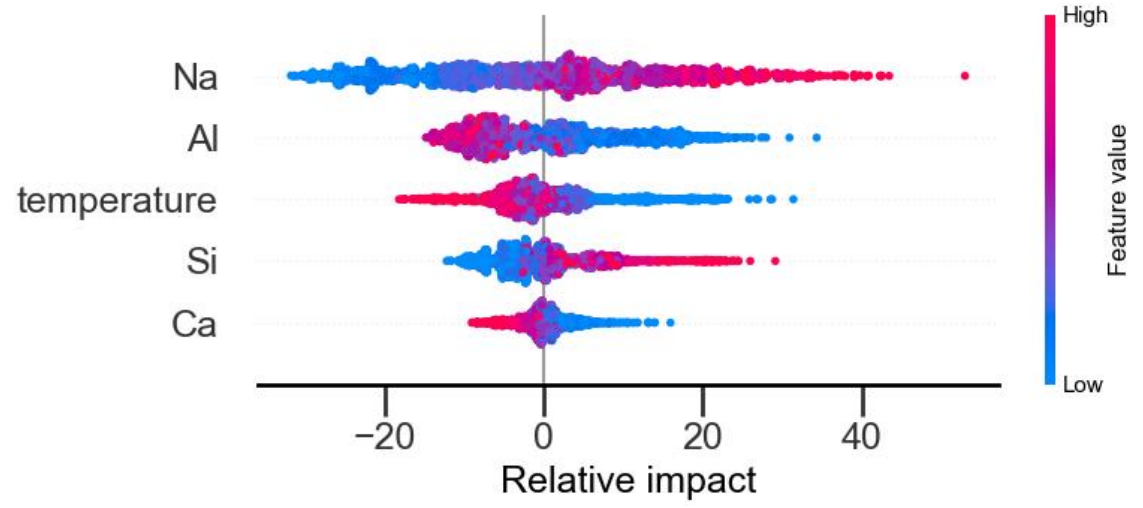

Figure 3.4-2

SHAP analysis of the GEMS data of ISG dissolution simulation. The relative impact indicates whether the feature will increase (positive) or decrease (negative) the precipitation-starting pH,

and the color bar shows this impact would happen with higher (red) or lower (blue) feature values. The vertical width of any distribution indicates the richness of data points.

3.5 Conclusion

In this chapter, we develop a complete methodology to predict zeolite precipitation in stage III of nuclear waste immobilization glass dissolution. Data from all parts are carefully validated by experimental results and are thus proved to be accurate and dependable. The AIMD methodology not only offers a route towards highly efficient harvesting of zeolite thermodynamic data, its treatment and understanding of the behavior of zeolitic water molecules also shed light on many earlier relevant topics and can be extended to the simulations of crystalline water molecules in other scenarios. The GEMS simulation combined with ML prediction will provide a simple and all machine-based data collection method that can greatly enrich the existing experimental records of zeolite synthesis. Finally, our work in this chapter is special in a way that it is never a complete version and would always benefit from more feeding data. As a result, we hope that future researchers can use this methodology as a starting point and keep ameliorate it towards the next generation of high-throughput simulation and data analysis.

4 Reference

(1) Varshneya, A. K. *Fundamentals of Inorganic Glasses*; Academic Press Inc, 1993.

(2) Zanotto, E. D.; Mauro, J. C. The Glassy State of Matter: Its Definition and Ultimate Fate. *J. Non-Cryst. Solids* **2017**, *471*, 490–495. https://doi.org/10.1016/j.jnoncrysol.2017.05.019.

(3) Sakka, S. Glasses and Glass-Ceramics from Gels. *J. Non-Cryst. Solids* **1985**, *73* (1–3), 651–660. https://doi.org/10.1016/0022-3093(85)90385-0.

(4) Gin, S. Open Scientific Questions about Nuclear Glass Corrosion. *Procedia Mater. Sci.* **2014**, *7*, 163–171. https://doi.org/10.1016/j.mspro.2014.10.022.

(5) Debenedetti, P. G.; Stillinger, F. H. Supercooled Liquids and the Glass Transition. *Nature* **2001**, *410* (6825), 259–267. https://doi.org/10.1038/35065704.

(6) Mauro, J. C.; Loucks, R. J. Forbidden Glasses and the Failure of Fictive Temperature. *J. Non-Cryst. Solids* **2009**, *355* (10), 676–680. https://doi.org/10.1016/j.jnoncrysol.2008.11.025.

(7) Zhao, Y. F.; Loo, S. C. J.; Chen, Y. Z.; Boey, F. Y. C.; Ma, J. In Situ SAXRD Study of Sol–Gel Induced Well-Ordered Mesoporous Bioglasses for Drug Delivery. *J. Biomed. Mater. Res. A* **2008**, *85A* (4), 1032–1042. https://doi.org/10.1002/jbm.a.31545.

(8) Kaur, G.; Pickrell, G.; Sriranganathan, N.; Kumar, V.; Homa, D. Review and the State of the Art: Sol–Gel and Melt Quenched Bioactive Glasses for Tissue Engineering. *J. Biomed. Mater. Res. B Appl. Biomater.* **2016**, *104* (6), 1248–1275. https://doi.org/10.1002/jbm.b.33443.

(9) Zanotto, E. D. The Formation of Unusual Glasses by Sol-Gel Processing. *J. Non-Cryst. Solids* **1992**, *147–148*, 820–823. https://doi.org/10.1016/S0022-3093(05)80723-9.

(10) Song, W.; Li, X.; Wang, B.; Krishnan, N. M. A.; Goyal, S.; Smedskjaer, M. M.; Mauro, J. C.; Bauchy, M. Atomic Picture of Structural Relaxation in Silicate Glasses. **2019**.

(11) Krishnan, N. M. A.; Wang, B.; Yu, Y.; Le Pape, Y.; Sant, G.; Bauchy, M. Enthalpy Landscape Dictates the Irradiation-Induced Disordering of Quartz. *Phys. Rev. X* **2017**, *7* (3), 031019. https://doi.org/10.1103/PhysRevX.7.031019.

(12) Ediger, M. D. Perspective: Highly Stable Vapor-Deposited Glasses. *J. Chem. Phys.* **2017**, *147* (21), 210901. https://doi.org/10.1063/1.5006265.

(13) Dutcher, J. R.; Ediger, M. D. Glass Surfaces Not So Glassy. *Science* **2008**, *319* (5863), 577–578. https://doi.org/10.1126/science.1155120.

(14) Dalal, S. S.; Ediger, M. D. Molecular Orientation in Stable Glasses of Indomethacin. *J. Phys. Chem. Lett.* **2012**, *3* (10), 1229–1233. https://doi.org/10.1021/jz3003266.

(15) Singh, S.; Ediger, M. D.; de Pablo, J. J. Ultrastable Glasses from *in Silico* Vapour Deposition. *Nat. Mater.* **2013**, *12* (2), 139–144. https://doi.org/10.1038/nmat3521.

(16) *Molecular Dynamics Simulations of Disordered Materials*; Massobrio, C., Du, J., Bernasconi, M., Salmon, P. S., Eds.; Springer Series in Materials Science; Springer International Publishing: Cham, 2015; Vol. 215. https://doi.org/10.1007/978-3-319-15675-0.

(17) Liu, Z.; Hu, Y.; Li, X.; Song, W.; Goyal, S.; Micoulaut, M.; Bauchy, M. Glass Relaxation and Hysteresis of the Glass Transition by Molecular Dynamics Simulations. *Phys. Rev. B* **2018**, *98* (10), 104205. https://doi.org/10.1103/PhysRevB.98.104205.

(18) Kresse, G.; Hafner, J. Ab Initio Molecular-Dynamics Simulation of the Liquid-Metal--Amorphous-Semiconductor Transition in Germanium. *Phys. Rev. B* **1994**, *49* (20), 14251–14269. https://doi.org/10.1103/PhysRevB.49.14251.

(19) Mischler, C.; Kob, W.; Binder, K. Classical and Ab-Initio Molecular Dynamic Simulation of an Amorphous Silica Surface. *Comput. Phys. Commun.* **2002**, *147* (1–2), 222–225. https://doi.org/10.1016/S0010-4655(02)00250-3.

(20) Le Roux, S.; Bouzid, A.; Boero, M.; Massobrio, C. Structural Properties of Glassy Ge 2 Se 3 from First-Principles Molecular Dynamics. *Phys. Rev. B* **2012**, *86* (22), 224201. https://doi.org/10.1103/PhysRevB.86.224201.

(21) Huang, L.; Kieffer, J. Thermomechanical Anomalies and Polyamorphism in B 2 O 3 Glass: A Molecular Dynamics Simulation Study. *Phys. Rev. B* **2006**, *74* (22), 224107. https://doi.org/10.1103/PhysRevB.74.224107.

(22) Goverapet Srinivasan, S.; van Duin, A. C. T. Molecular-Dynamics-Based Study of the Collisions of Hyperthermal Atomic Oxygen with Graphene Using the ReaxFF Reactive Force Field. *J. Phys. Chem. A* **2011**, *115* (46), 13269–13280. https://doi.org/10.1021/jp207179x.

(23) Benoit, M.; Ispas, S.; Jund, P.; Jullien, R. Model of Silica Glass from Combined Classical and Ab Initio Molecular-Dynamics Simulations. *Eur. Phys. J. B* **2000**, *13* (4), 631–636. https://doi.org/10.1007/s100510050079.

(24) Aktulga, H. M.; Fogarty, J. C.; Pandit, S. A.; Grama, A. Y. Parallel Reactive Molecular Dynamics: Numerical Methods and Algorithmic Techniques. *Parallel Comput.* **2012**, *38* (4–5), 245–259. https://doi.org/10.1016/j.parco.2011.08.005.

(25) Li, X.; Song, W.; Yang, K.; Krishnan, N. M. A.; Wang, B.; Smedskjaer, M. M.; Mauro, J. C.; Sant, G.; Balonis, M.; Bauchy, M. Cooling Rate Effects in Sodium Silicate Glasses: Bridging the Gap between Molecular Dynamics Simulations and Experiments. *J. Chem. Phys.* **2017**, *147* (7), 074501. https://doi.org/10.1063/1.4998611.

(26) Yu, Y.; Wang, B.; Wang, M.; Sant, G.; Bauchy, M. Revisiting Silica with ReaxFF: Towards Improved Predictions of Glass Structure and Properties via Reactive Molecular Dynamics. *J. Non-Cryst. Solids* **2016**, *443*, 148–154. https://doi.org/10.1016/j.jnoncrysol.2016.03.026.

(27) Cobb, M.; Drabold, D. A.; Cappelletti, R. L. *Ab Initio* Molecular-Dynamics Study of the Structural, Vibrational, and Electronic Properties of Glassy GeSe 2. *Phys. Rev. B* **1996**, *54* (17), 12162–12171. https://doi.org/10.1103/PhysRevB.54.12162.

(28) *Revisiting silica with ReaxFF: Towards improved predictions of glass structure and properties via reactive molecular dynamics - ScienceDirect*. https://www.sciencedirect.com/science/article/pii/S0022309316300758 (accessed 2019-01-22).

(29) Yu, Y.; Wang, B.; Wang, M.; Sant, G.; Bauchy, M. Reactive Molecular Dynamics Simulations of Sodium Silicate Glasses - Toward an Improved Understanding of the Structure. *Int. J. Appl. Glass Sci.* **2017**, *8* (3), 276–284. https://doi.org/10.1111/ijag.12248.

(30) Narayanasamy, S.; Jollivet, P.; Godon, N.; Angeli, F.; Gin, S.; Cabié, M.; Cambedouzou, J.; Le Guillou, C.; Abdelouas, A. Influence of Composition of Nuclear Waste Glasses on Vapor Phase Hydration. *J. Nucl. Mater.* **2019**, *525*, 53–71. https://doi.org/10.1016/j.jnucmat.2019.07.015.

(31) Pegg, I. L. Turning Nuclear Waste into Glass. *Phys. Today* **2015**, *68* (2), 33–39. https://doi.org/10.1063/PT.3.2687.

(32) Wang, Z.; Zhen, B.; Venkatesh, P.; Sant, G.; Bauchy, M. *Decoding Zeolite Crystallization and Stage III in Nuclear Waste Glasses by Coupled Modeling and Experiments*; DOE DOE report 18-15020; Department of civil and environmental engineering, University of California, Los Angeles, 2019; p 23.

(33) Zhen-Wu, B. Y.; Prentice, D. P.; Simonetti, D.; Ryan, J. V.; Sant, G.; Bauchy, M. Predicting Zeolites' Stability during the Corrosion of Nuclear Waste Immobilization Glasses: Comparison with Glass Corrosion Experiments. *J. Nucl. Mater.* **2021**, *547*, 152813. https://doi.org/10.1016/j.jnucmat.2021.152813.

(34) *Key Issues: Disposal of High-Level Nuclear Waste*. https://www.gao.gov/key_issues/disposal_of_highlevel_nuclear_waste/issue_summary (accessed 2019-09-03).

(35) Gin, S.; Mestre, J. P. SON 68 Nuclear Glass Alteration Kinetics between PH 7 and PH 11.5. *J. Nucl. Mater.* **2001**, *295* (1), 83–96. https://doi.org/10.1016/S0022-3115(01)00434-2.

(36) Gin, S.; Jollivet, P.; Fournier, M.; Berthon, C.; Wang, Z.; Mitroshkov, A.; Zhu, Z.; Ryan, J. V. The Fate of Silicon during Glass Corrosion under Alkaline Conditions: A Mechanistic and Kinetic Study with the International Simple Glass. *Geochim. Cosmochim. Acta* **2015**, *151*, 68–85. https://doi.org/10.1016/j.gca.2014.12.009.

(37) Gin, S.; Jollivet, P.; Fournier, M.; Berthon, C.; Wang, Z.; Mitroshkov, A.; Zhu, Z.; Ryan, J. V. The Fate of Silicon during Glass Corrosion under Alkaline Conditions: A Mechanistic and Kinetic Study with the International Simple Glass. *Geochim. Cosmochim. Acta* **2015**, *151*, 68–85. https://doi.org/10.1016/j.gca.2014.12.009.

(38) Fournier, M.; Gin, S.; Frugier, P. Resumption of Nuclear Glass Alteration: State of the Art. *J. Nucl. Mater.* **2014**, *448* (1–3), 348–363. https://doi.org/10.1016/j.jnucmat.2014.02.022.

(39) Du, T.; Li, H.; Sant, G.; Bauchy, M. New Insights into the Sol–Gel Condensation of Silica by Reactive Molecular Dynamics Simulations. *J. Chem. Phys.* **2018**, *148* (23), 234504. https://doi.org/10.1063/1.5027583.

(40) Swallen, S. F.; Kearns, K. L.; Mapes, M. K.; Kim, Y. S.; McMahon, R. J.; Ediger, M. D.; Wu, T.; Yu, L.; Satija, S. Organic Glasses with Exceptional Thermodynamic and Kinetic Stability. *Science* **2007**, *315* (5810), 353–356. https://doi.org/10.1126/science.1135795.

(41) Kearns, K. L.; Swallen, S. F.; Ediger, M. D.; Wu, T.; Yu, L. Influence of Substrate Temperature on the Stability of Glasses Prepared by Vapor Deposition. *J. Chem. Phys.* **2007**, *127* (15), 154702. https://doi.org/10.1063/1.2789438.

(42) Kearns, K. L.; Swallen, S. F.; Ediger, M. D.; Wu, T.; Sun, Y.; Yu, L. Hiking down the Energy Landscape: Progress Toward the Kauzmann Temperature via Vapor Deposition. *J. Phys. Chem. B* **2008**, *112* (16), 4934–4942. https://doi.org/10.1021/jp7113384.

(43) Dalal, S. S.; Walters, D. M.; Lyubimov, I.; Pablo, de J. J.; Ediger, M. D. Tunable Molecular Orientation and Elevated Thermal Stability of Vapor-Deposited Organic Semiconductors. *Proc. Natl. Acad. Sci.* **2015**, *112* (14), 4227–4232. https://doi.org/10.1073/pnas.1421042112.

(44) Reid, D. R.; Lyubimov, I.; Ediger, M. D.; de Pablo, J. J. Age and Structure of a Model Vapour-Deposited Glass. *Nat. Commun.* **2016**, *7*, 13062. https://doi.org/10.1038/ncomms13062.

(45) Berthier, L.; Charbonneau, P.; Flenner, E.; Zamponi, F. Origin of Ultrastability in Vapor-Deposited Glasses. *Phys. Rev. Lett.* **2017**, *119* (18), 188002. https://doi.org/10.1103/PhysRevLett.119.188002.

(46) Phiriyawirut, P.; Magaraphan, R.; Jamieson, A. M.; Wongkasemjit, S. MFI Zeolite Synthesis Directly from Silatrane via Sol–Gel Process and Microwave Technique. *Mater. Sci. Eng. A* **2003**, *361* (1–2), 147–154. https://doi.org/10.1016/S0921-5093(03)00509-4.

(47) Jones, J. R. Review of Bioactive Glass: From Hench to Hybrids. *Acta Biomater.* **2013**, *9* (1), 4457–4486. https://doi.org/10.1016/j.actbio.2012.08.023.

(48) Mackenzie, J. D. Glasses from Melts and Glasses from Gels, a Comparison. *J. Non-Cryst. Solids* **1982**, *48* (1), 1–10. https://doi.org/10.1016/0022-3093(82)90241-1.

(49) Garofalini, S. H.; Martin, G. Molecular Simulations of the Polymerization of Silicic Acid Molecules and Network Formation. *J. Phys. Chem.* **1994**, *98* (4), 1311–1316. https://doi.org/10.1021/j100055a044.

(50) Malani, A.; Auerbach, S. M.; Monson, P. A. Monte Carlo Simulations of Silica Polymerization and Network Formation. *J. Phys. Chem. C* **2011**, *115* (32), 15988–16000. https://doi.org/10.1021/jp202209g.

(51) Deetz, J. D.; Faller, R. Reactive Modeling of the Initial Stages of Alkoxysilane Polycondensation: Effects of Precursor Molecule Structure and Solution Composition. *Soft Matter* **2015**, *11* (34), 6780–6789. https://doi.org/10.1039/C5SM00964B.

(52) Rao, N. Z.; Gelb, L. D. Molecular Dynamics Simulations of the Polymerization of Aqueous Silicic Acid and Analysis of the Effects of Concentration on Silica Polymorph Distributions, Growth Mechanisms, and Reaction Kinetics. *J. Phys. Chem. B* **2004**, *108* (33), 12418–12428. https://doi.org/10.1021/jp049169f.

(53) Gnado, J.; Dhamelincourt, P.; Pélégris, C.; Traisnel, M.; Le Maguer Mayot, A. Raman Spectra of Oligomeric Species Obtained by Tetraethoxysilane Hydrolysis-Polycondensation Process. *J. Non-Cryst. Solids* **1996**, *208* (3), 247–258. https://doi.org/10.1016/S0022-3093(96)00526-1.

(54) Bhattacharya, S.; Kieffer, J. Molecular Dynamics Simulation Study of Growth Regimes during Polycondensation of Silicic Acid: From Silica Nanoparticles to Porous Gels. *J. Phys. Chem. C* **2008**, *112* (6), 1764–1771. https://doi.org/10.1021/jp073808f.

(55) Rimsza, J. M.; Yeon, J.; van Duin, A. C. T.; Du, J. Water Interactions with Nanoporous Silica: Comparison of ReaxFF and *Ab Initio* Based Molecular Dynamics Simulations. *J. Phys. Chem. C* **2016**, *120* (43), 24803–24816. https://doi.org/10.1021/acs.jpcc.6b07939.

(56) van Duin, A. C. T.; Strachan, A.; Stewman, S.; Zhang, Q.; Xu, X.; Goddard, W. A. ReaxFF $_{SiO}$ Reactive Force Field for Silicon and Silicon Oxide Systems. *J. Phys. Chem. A* **2003**, *107* (19), 3803–3811. https://doi.org/10.1021/jp0276303.

(57) Trachenko, K. Understanding Resistance to Amorphization by Radiation Damage. *J. Phys. Condens. Matter* **2004**, *16* (49), R1491–R1515. https://doi.org/10.1088/0953-8984/16/49/R03.

(58) Sickafus, K. E.; Grimes, R. W.; Valdez, J. A.; Cleave, A.; Tang, M.; Ishimaru, M.; Corish, S. M.; Stanek, C. R.; Uberuaga, B. P. Radiation-Induced Amorphization Resistance and Radiation Tolerance in Structurally Related Oxides. *Nat. Mater.* **2007**, *6* (3), 217–223. https://doi.org/10.1038/nmat1842.

(59) Sickafus, K. E.; Minervini, L.; Grimes, R. W.; Valdez, J. A.; Ishimaru, M.; Li, F.; McClellan, K. J.; Hartmann, T. Radiation Tolerance of Complex Oxides. *Science* **2000**, *289* (5480), 748–751. https://doi.org/10.1126/science.289.5480.748.

(60) Schulz, M. Ion Implantation: A Useful Tool for Semiconductor Research. *Appl. Phys.* **1974**, *4* (2), 91–104. https://doi.org/10.1007/BF00884263.

(61) Stoneham, A. M.; Matthews, J. R.; Ford, I. J. Innovative Materials for Fusion Power Plant Structures: Separating Functions. *J. Phys. Condens. Matter* **2004**, *16* (27), S2597–S2621. https://doi.org/10.1088/0953-8984/16/27/001.

(62) Schneider, T.; Stoll, E. Molecular-Dynamics Study of a Three-Dimensional One-Component Model for Distortive Phase Transitions. *Phys. Rev. B* **1978**, *17* (3), 1302–1322. https://doi.org/10.1103/PhysRevB.17.1302.

(63) Bitzek, E.; Koskinen, P.; Gähler, F.; Moseler, M.; Gumbsch, P. Structural Relaxation Made Simple. *Phys. Rev. Lett.* **2006**, *97* (17). https://doi.org/10.1103/PhysRevLett.97.170201.

(64) Fogarty, J. C.; Aktulga, H. M.; Grama, A. Y.; van Duin, A. C. T.; Pandit, S. A. A Reactive Molecular Dynamics Simulation of the Silica-Water Interface. *J. Chem. Phys.* **2010**, *132* (17), 174704. https://doi.org/10.1063/1.3407433.

(65) van Duin, A. C. T.; Dasgupta, S.; Lorant, F.; Goddard, W. A. ReaxFF: A Reactive Force Field for Hydrocarbons. *J. Phys. Chem. A* **2001**, *105* (41), 9396–9409. https://doi.org/10.1021/jp004368u.

(66) Meng, L.; Sun, Q.; Wang, J.; Ding, F. Molecular Dynamics Simulation of Chemical Vapor Deposition Graphene Growth on Ni (111) Surface. *J. Phys. Chem. C* **2012**, *116* (10), 6097–6102. https://doi.org/10.1021/jp212149c.

(67) Plimpton, S. Fast Parallel Algorithms for Short-Range Molecular Dynamics. *J. Comput. Phys.* **1995**, *117* (1), 1–19. https://doi.org/10.1006/jcph.1995.1039.

(68) Pignatelli, I.; Kumar, A.; Field, K. G.; Wang, B.; Yu, Y.; Le Pape, Y.; Bauchy, M.; Sant, G. Direct Experimental Evidence for Differing Reactivity Alterations of Minerals Following Irradiation: The Case of Calcite and Quartz. *Sci. Rep.* **2016**, *6* (1), 20155. https://doi.org/10.1038/srep20155.

(69) Wang, B.; Yu, Y.; Pignatelli, I.; Sant, G.; Bauchy, M. Nature of Radiation-Induced Defects in Quartz. *J. Chem. Phys.* **2015**, *143* (2), 024505. https://doi.org/10.1063/1.4926527.

(70) Weber, W. J. Radiation-Induced Defects and Amorphization in Zircon. *J. Mater. Res.* **1990**, *5* (11), 2687–2697. https://doi.org/10.1557/JMR.1990.2687.

(71) Hoover, W. G. Canonical Dynamics: Equilibrium Phase-Space Distributions. *Phys. Rev. A* **1985**, *31* (3), 1695–1697. https://doi.org/10.1103/PhysRevA.31.1695.

(72) Manzano, H.; Moeini, S.; Marinelli, F.; van Duin, A. C. T.; Ulm, F.-J.; Pellenq, R. J.-M. Confined Water Dissociation in Microporous Defective Silicates: Mechanism, Dipole Distribution, and Impact on Substrate Properties. *J. Am. Chem. Soc.* **2012**, *134* (4), 2208–2215. https://doi.org/10.1021/ja209152n.

(73) Senftle, T. P.; Hong, S.; Islam, M. M.; Kylasa, S. B.; Zheng, Y.; Shin, Y. K.; Junkermeier, C.; Engel-Herbert, R.; Janik, M. J.; Aktulga, H. M.; Verstraelen, T.; Grama, A.; van Duin, A. C. T. The ReaxFF Reactive Force-Field: Development, Applications and Future Directions. *Npj Comput. Mater.* **2016**, *2* (1), 15011. https://doi.org/10.1038/npjcompumats.2015.11.

(74) Rappe, A. K.; Goddard, W. A. Charge Equilibration for Molecular Dynamics Simulations. *J. Phys. Chem.* **1991**, *95* (8), 3358–3363. https://doi.org/10.1021/j100161a070.

(75) Demiralp, E.; Çağin, T.; Goddard, W. A. Morse Stretch Potential Charge Equilibrium Force Field for Ceramics: Application to the Quartz-Stishovite Phase Transition and to Silica Glass. *Phys. Rev. Lett.* **1999**, *82* (8), 1708–1711. https://doi.org/10.1103/PhysRevLett.82.1708.

(76) Yu, Y.; Krishnan, N. M. A.; Smedskjaer, M. M.; Sant, G.; Bauchy, M. The Hydrophilic-to-Hydrophobic Transition in Glassy Silica Is Driven by the Atomic Topology of Its Surface. *J. Chem. Phys.* **2018**, *148* (7), 074503. https://doi.org/10.1063/1.5010934.

(77) Yeon, J.; van Duin, A. C. T. ReaxFF Molecular Dynamics Simulations of Hydroxylation Kinetics for Amorphous and Nano-Silica Structure, and Its Relations with Atomic Strain Energy. *J. Phys. Chem. C* **2016**, *120* (1), 305–317. https://doi.org/10.1021/acs.jpcc.5b09784.

(78) Smedskjaer, M. M.; Bauchy, M.; Mauro, J. C.; Rzoska, S. J.; Bockowski, M. Unique Effects of Thermal and Pressure Histories on Glass Hardness: Structural and Topological Origin. *J. Chem. Phys.* **2015**, *143* (16), 164505. https://doi.org/10.1063/1.4934540.

(79) Krishnan, N. M. A.; Wang, B.; Le Pape, Y.; Sant, G.; Bauchy, M. Irradiation-Driven Amorphous-to-Glassy Transition in Quartz: The Crucial Role of the Medium-Range Order in Crystallization. *Phys. Rev. Mater.* **2017**, *1* (5), 053405. https://doi.org/10.1103/PhysRevMaterials.1.053405.

(80) Lyubimov, I.; Ediger, M. D.; de Pablo, J. J. Model Vapor-Deposited Glasses: Growth Front and Composition Effects. *J. Chem. Phys.* **2013**, *139* (14), 144505. https://doi.org/10.1063/1.4823769.

(81) Donati, C.; Glotzer, S. C.; Poole, P. H.; Kob, W.; Plimpton, S. J. Spatial Correlations of Mobility and Immobility in a Glass-Forming Lennard-Jones Liquid. *Phys. Rev. E* **1999**, *60* (3), 3107–3119. https://doi.org/10.1103/PhysRevE.60.3107.

(82) Lin, P.-H.; Lyubimov, I.; Yu, L.; Ediger, M. D.; de Pablo, J. J. Molecular Modeling of Vapor-Deposited Polymer Glasses. *J. Chem. Phys.* **2014**, *140* (20), 204504. https://doi.org/10.1063/1.4876078.

(83) Sun, G.; Saw, S.; Douglass, I.; Harrowell, P. Structural Origin of Enhanced Dynamics at the Surface of a Glassy Alloy. *Phys. Rev. Lett.* **2017**, *119* (24). https://doi.org/10.1103/PhysRevLett.119.245501.

(84) Bauchy, M.; Guillot, B.; Micoulaut, M.; Sator, N. Viscosity and Viscosity Anomalies of Model Silicates and Magmas: A Numerical Investigation. *Chem. Geol.* **2013**, *346*, 47–56. https://doi.org/10.1016/j.chemgeo.2012.08.035.

(85) Bauchy, M.; Micoulaut, M. From Pockets to Channels: Density-Controlled Diffusion in Sodium Silicates. *Phys. Rev. B* **2011**, *83* (18), 184118. https://doi.org/10.1103/PhysRevB.83.184118.

(86) Brian, C. W.; Yu, L. Surface Self-Diffusion of Organic Glasses. *J. Phys. Chem. A* **2013**, *117* (50), 13303–13309. https://doi.org/10.1021/jp404944s.

(87) Micoulaut, M.; Phillips, J. C. Rings and Rigidity Transitions in Network Glasses. *Phys. Rev. B* **2003**, *67* (10). https://doi.org/10.1103/PhysRevB.67.104204.

(88) Geissberger, A. E.; Galeener, F. L. Raman Studies of Vitreous Si${\mathrm{O}}_{2}$ versus Fictive Temperature. *Phys. Rev. B* **1983**, *28* (6), 3266–3271. https://doi.org/10.1103/PhysRevB.28.3266.

(89) Le Roux, S.; Jund, P. Ring Statistics Analysis of Topological Networks: New Approach and Application to Amorphous GeS2 and SiO2 Systems. *Comput. Mater. Sci.* **2010**, *49* (1), 70–83. https://doi.org/10.1016/j.commatsci.2010.04.023.

(90) Elliott, S. R. Medium-Range Structural Order in Covalent Amorphous Solids. *Nature* **1991**, *354* (6353), 445–452. https://doi.org/10.1038/354445a0.

(91) Jiang, J.; Walters, D. M.; Zhou, D.; Ediger, M. D. Substrate Temperature Controls Molecular Orientation in Two-Component Vapor-Deposited Glasses. *Soft Matter* **2016**, *12* (13), 3265–3270. https://doi.org/10.1039/C6SM00262E.

(92) Lyubimov, I.; Antony, L.; Walters, D. M.; Rodney, D.; Ediger, M. D.; de Pablo, J. J. Orientational Anisotropy in Simulated Vapor-Deposited Molecular Glasses. *J. Chem. Phys.* **2015**, *143* (9), 094502. https://doi.org/10.1063/1.4928523.

(93) Barkema, G. T.; Mousseau, N. Event-Based Relaxation of Continuous Disordered Systems. *Phys. Rev. Lett.* **1996**, *77* (21), 4358–4361. https://doi.org/10.1103/PhysRevLett.77.4358.

(94) Cancès, E.; Legoll, F.; Marinica, M.-C.; Minoukadeh, K.; Willaime, F. Some Improvements of the Activation-Relaxation Technique Method for Finding Transition Pathways on Potential Energy Surfaces. *J. Chem. Phys.* **2009**, *130* (11), 114711. https://doi.org/10.1063/1.3088532.

(95) Fan, Y.; Iwashita, T.; Egami, T. Energy Landscape-Driven Non-Equilibrium Evolution of Inherent Structure in Disordered Material. *Nat. Commun.* **2017**, *8* (1), 15417. https://doi.org/10.1038/ncomms15417.

(96) Micoulaut, M.; Kachmar, A.; Bauchy, M.; Le Roux, S.; Massobrio, C.; Boero, M. Structure, Topology, Rings, and Vibrational and Electronic Properties of Ge x Se 1 − x Glasses across the Rigidity Transition: A Numerical Study. *Phys. Rev. B* **2013**, *88* (5), 054203. https://doi.org/10.1103/PhysRevB.88.054203.

(97) Johnson, G. K. (Argonne N. L.; Flotow, H. E.; O'Hare, P. a. G.; Wise, W. S. Thermodynamic Studies of Zeolites: Analcime and Dehydrated Analcime. *Am Miner. U. S.* **1982**, *67:7-8*.

(98) Line, C. M. B.; Winkler, B.; Dove, M. T. Quasielastic Incoherent Neutron Scattering Study of the Rotational Dynamics of the Water Molecules in Analcime. *Phys. Chem. Miner.* **1994**, *21* (7). https://doi.org/10.1007/BF00202275.

(99) Line, C. M. B.; Dove, M. T.; Knight, K. S.; Winkler, B. The Low-Temperature Behaviour of Analcime. 1: High-Resolution Neutron Powder Diffraction. *Mineral. Mag.* **1996**, *60* (400), 499–507. https://doi.org/10.1180/minmag.1996.060.400.11.

(100) Johnson, G. K.; Flotow, H. E.; O'Hare, P. a. G.; Wise, W. S. Thermodynamic Studies of Zeolites; Natrolite, Mesolite and Scolecite. *Am. Mineral.* **1983**, *68* (11–12), 1134–1145.

(101) Kiseleva, I.; Navrotsky, A.; Belitsky, I. A.; Fursenko, B. A. Thermochemistry and Phase Equilibria in Calcium Zeolites. *Am. Mineral.* **2015**, *81* (5–6), 658–667. https://doi.org/10.2138/am-1996-5-613.

(102) Mathieu, R.; Vieillard, P. A Predictive Model for the Enthalpies of Formation of Zeolites. *Microporous Mesoporous Mater.* **2010**, *132* (3), 335–351. https://doi.org/10.1016/j.micromeso.2010.03.011.

(103) Vieillard, P. A Predictive Model for the Entropies and Heat Capacities of Zeolites. *Eur. J. Mineral.* **2010**, *22* (6), 823–836. https://doi.org/10.1127/0935-1221/2010/0022-2026.

(104) Glaccum, R.; Boström, K. (Na, K)-Phillipsite: Its Stability Conditions and Geochemical Role in the Deep Sea. *Mar. Geol.* **1976**, *21* (1), 47–58. https://doi.org/10.1016/0025-3227(76)90103-1.

(105) Johnson, G. K. Thermodynamic Studies of Zeolites: Clinoptilolite a. 10.

(106) Kiseleva, I.; Navrotsky, A.; Belitsky, I.; Fursenko, B. Thermochemical Study of Calcium Zeolites—Heulandite and Stilbite. *Am. Mineral.* **2001**, *86* (4), 448–455. https://doi.org/10.2138/am-2001-0408.

(107) Kiseleva, I. A.; Ogorodova, L. P.; Melchakova, L. V.; Belitsky, I. A.; Fursenko, B. A. Thermochemical Investigation of Natural Fibrous Zeolites. *Eur. J. Mineral.* **1997**, 327–332. https://doi.org/10.1127/ejm/9/2/0327.

(108) Yang, K.; Oses, C.; Curtarolo, S. Modeling Off-Stoichiometry Materials with a High-Throughput Ab-Initio Approach. *Chem. Mater.* **2016**, *28* (18), 6484–6492. https://doi.org/10.1021/acs.chemmater.6b01449.

(109) Kresse, G.; Hafner, J. Ab Initio Molecular Dynamics for Liquid Metals. *Phys. Rev. B* **1993**, *47* (1), 558–561. https://doi.org/10.1103/PhysRevB.47.558.

(110) Kresse, G.; Furthmüller, J. Efficiency of Ab-Initio Total Energy Calculations for Metals and Semiconductors Using a Plane-Wave Basis Set. *Comput. Mater. Sci.* **1996**, *6* (1), 15–50. https://doi.org/10.1016/0927-0256(96)00008-0.

(111) Kresse, G.; Furthmüller, J. Efficient Iterative Schemes for Ab Initio Total-Energy Calculations Using a Plane-Wave Basis Set. *Phys. Rev. B* **1996**, *54* (16), 11169–11186. https://doi.org/10.1103/PhysRevB.54.11169.

(112) Togo, A.; Tanaka, I. First Principles Phonon Calculations in Materials Science. *Scr. Mater.* **2015**, *108*, 1–5. https://doi.org/10.1016/j.scriptamat.2015.07.021.

(113) Perdew, J. P.; Burke, K.; Ernzerhof, M. Generalized Gradient Approximation Made Simple. *Phys. Rev. Lett.* **1996**, *77* (18), 3865–3868. https://doi.org/10.1103/PhysRevLett.77.3865.

(114) Langreth, D. C.; Mehl, M. J. Beyond the Local-Density Approximation in Calculations of Ground-State Electronic Properties. *Phys. Rev. B* **1983**, *28* (4), 1809–1834. https://doi.org/10.1103/PhysRevB.28.1809.

(115) Robson, H. *Verified Synthesis of Zeolitic Materials: Second Edition*; Gulf Professional Publishing, 2001.

(116) Jain, A.; Ong, S. P.; Hautier, G.; Chen, W.; Richards, W. D.; Dacek, S.; Cholia, S.; Gunter, D.; Skinner, D.; Ceder, G.; Persson, K. A. Commentary: The Materials Project: A Materials Genome Approach to Accelerating Materials Innovation. *APL Mater.* **2013**, *1* (1), 011002. https://doi.org/10.1063/1.4812323.

(117) Pitman, M. C.; van Duin, A. C. T. Dynamics of Confined Reactive Water in Smectite Clay–Zeolite Composites. *J. Am. Chem. Soc.* **2012**, *134* (6), 3042–3053. https://doi.org/10.1021/ja208894m.

(118) Ong, S. P.; Richards, W. D.; Jain, A.; Hautier, G.; Kocher, M.; Cholia, S.; Gunter, D.; Chevrier, V. L.; Persson, K. A.; Ceder, G. Python Materials Genomics (Pymatgen): A Robust, Open-Source Python Library for Materials Analysis. *Comput. Mater. Sci.* **2013**, *68*, 314–319. https://doi.org/10.1016/j.commatsci.2012.10.028.

(119) Togo, A.; Chaput, L.; Tanaka, I.; Hug, G. First-Principles Phonon Calculations of Thermal Expansion in Ti 3 SiC 2 , Ti 3 AlC 2 , and Ti 3 GeC 2. *Phys. Rev. B* **2010**, *81* (17). https://doi.org/10.1103/PhysRevB.81.174301.

(120) Parlinski, K.; Li, Z. Q.; Kawazoe, Y. First-Principles Determination of the Soft Mode in Cubic ${\mathrm{ZrO}}_{2}$. *Phys. Rev. Lett.* **1997**, *78* (21), 4063–4066. https://doi.org/10.1103/PhysRevLett.78.4063.

(121) Chaput, L.; Togo, A.; Tanaka, I.; Hug, G. Phonon-Phonon Interactions in Transition Metals. *Phys. Rev. B* **2011**, *84* (9). https://doi.org/10.1103/PhysRevB.84.094302.

(122) Dove, M. T.; Dove, M. T. *Introduction to Lattice Dynamics*; Cambridge University Press, 1993.

(123) Farimani, A. B.; Wu, Y.; Aluru, N. R. Rotational Motion of a Single Water Molecule in a Buckyball. *Phys. Chem. Chem. Phys.* **2013**, *15* (41), 17993. https://doi.org/10.1039/c3cp53277a.

(124) Lieb, E. H.; Yngvason, J. The Physics and Mathematics of the Second Law of Thermodynamics. *Phys. Rep.* **1999**, *310* (1), 1–96. https://doi.org/10.1016/S0370-1573(98)00082-9.

(125) Widom, B. *Statistical Mechanics: A Concise Introduction for Chemists*; Cambridge University Press: Cambridge, 2002. https://doi.org/10.1017/CBO9780511815836.

(126) Dey, P.; Nazarov, R.; Dutta, B.; Yao, M.; Herbig, M.; Friák, M.; Hickel, T.; Raabe, D.; Neugebauer, J. *Ab Initio* Explanation of Disorder and off-Stoichiometry in Fe-Mn-Al-C κ Carbides. *Phys. Rev. B* **2017**, *95* (10), 104108. https://doi.org/10.1103/PhysRevB.95.104108.

(127) Gopal, C. B.; van de Walle, A. *Ab Initio* Thermodynamics of Intrinsic Oxygen Vacancies in Ceria. *Phys. Rev. B* **2012**, *86* (13). https://doi.org/10.1103/PhysRevB.86.134117.

(128) Hart, G. L. W.; Forcade, R. W. Algorithm for Generating Derivative Structures. *Phys. Rev. B* **2008**, *77* (22), 224115. https://doi.org/10.1103/PhysRevB.77.224115.

(129) *Thermodynamics of Dehydration and Hydration in Natrolite and Analcime*. https://ufdc.ufl.edu/UFE0015761/00001 (accessed 2019-07-20).

(130) Line, C. M. B.; Kearley, G. J.; Suard, E.; Fitch, A.; Swainson, I. Water in Wairakite: A Water-Zeolite Model System. *Phys. B Condens. Matter* **1997**, *234–236*, 79–81. https://doi.org/10.1016/S0921-4526(96)00887-3.

(131) Johnson, G. K. (Argonne N. L.; Flotow, H. E.; O'Hare, P. a. G.; Wise, W. S. Thermodynamic Studies of Zeolites: Analcime and Dehydrated Analcime. *Am Miner. U. S.* **1982**, *67:7-8*.

(132) Zhen-Wu, B. Y.; Prentice, D. P.; Ryan, J. V.; Ellison, K.; Bauchy, M.; Sant, G. Zeo19: A Thermodynamic Database for Assessing Zeolite Stability during the Corrosion of Nuclear

Waste Immobilization Glasses. *Npj Mater. Degrad.* **2020**, *4* (1). https://doi.org/10.1038/s41529-019-0106-1.

(133) JonNsoN, G. K.; Tasrr, I. R.; Fr-orow, H. E.; O'Hlnr, P. A. G. Thermodynamic Studies of Mordenite, Dehydrated Mordenite, and Gibbsite. 9.

(134) Frank, H. S.; Evans, M. W. Free Volume and Entropy in Condensed Systems III. Entropy in Binary Liquid Mixtures; Partial Molal Entropy in Dilute Solutions; Structure and Thermodynamics in Aqueous Electrolytes. *J. Chem. Phys.* **1945**, *13* (11), 507–532. https://doi.org/10.1063/1.1723985.

(135) Cohen, M. H.; Grest, G. S. Liquid-Glass Transition, a Free-Volume Approach. *Phys. Rev. B* **1979**, *20* (3), 1077–1098. https://doi.org/10.1103/PhysRevB.20.1077.

(136) Naumis, G. G. Energy Landscape and Rigidity. *Phys. Rev. E* **2005**, *71* (2), 026114. https://doi.org/10.1103/PhysRevE.71.026114.

(137) Handle, P. H.; Sciortino, F. The Adam–Gibbs Relation and the TIP4P/2005 Model of Water. *Mol. Phys.* **2018**, *116* (21–22), 3366–3371. https://doi.org/10.1080/00268976.2018.1471230.

(138) Miller, A. A. ``Free Volume'' and the Viscosity of Liquid Water. *J. Chem. Phys.* **1963**, *38* (7), 1568–1571. https://doi.org/10.1063/1.1776922.

(139) Cabane, B.; Vuilleumier, R. The Physics of Liquid Water. 24.

(140) Zhen-Wu, B. Y.; Prentice, D. P.; Ryan, J. V.; Ellison, K.; Bauchy, M.; Sant, G. Zeo19: A Thermodynamic Database for Assessing Zeolite Stability during the Corrosion of Nuclear

Waste Immobilization Glasses. *Npj Mater. Degrad.* **2020**, *4* (1). https://doi.org/10.1038/s41529-019-0106-1.

(141) Wagner, T.; Kulik, D. A.; Hingerl, F. F.; Dmytrieva, S. V. GEM-Selektor Geochemical Modeling Package: TSolMod Library and Data Interface for Multicomponent Phase Models. *Can. Mineral.* **2012**, *50* (5), 1173–1195.

(142) Kulik, D. A.; Wagner, T.; Dmytrieva, S. V.; Kosakowski, G.; Hingerl, F. F.; Chudnenko, K. V.; Berner, U. R. GEM-Selektor Geochemical Modeling Package: Revised Algorithm and GEMS3K Numerical Kernel for Coupled Simulation Codes. *Comput. Geosci.* **2013**, *17* (1), 1–24.

(143) Beauvais, C.; Boutin, A.; Fuchs, A. H. Adsorption of Water in Zeolite Sodium-Faujasite. *Comptes Rendus Chim.* **2005**, *8* (3–4), 485–490. https://doi.org/10.1016/j.crci.2004.11.011.

(144) Bhatia, S. *Zeolite Catalysts: Principles and Applications*; 2020.

(145) Krishna, R. Investigation of Entropy Effects during Sorption of Mixtures of Alkanes in MFI Zeolite. *Chem. Eng. J.* **2002**, *88* (1–3), 81–94. https://doi.org/10.1016/S1385-8947(01)00253-4.